OCS Study
BOEM 2025-005

Impact of Non-linear Sedimentation on Dredge Area Benthic Ecosystem on the Louisiana Shelf

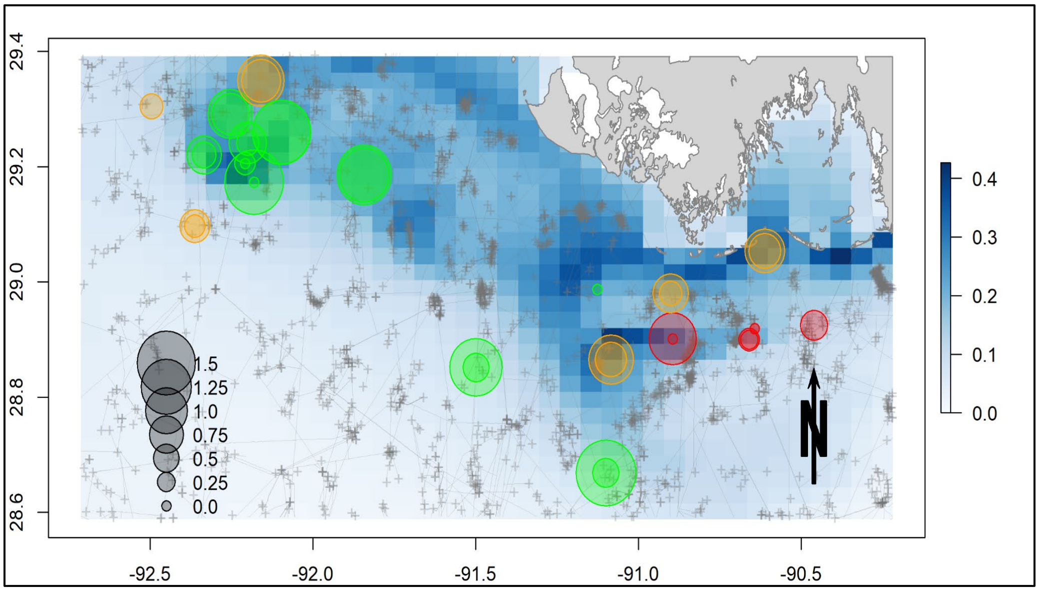

U.S. Department of the Interior
Bureau of Ocean Energy Management
Gulf of Mexico Regional Office
New Orleans, LA

OCS Study
BOEM 2025-005

Impact of Non-linear Sedimentation on Dredge Area Benthic Ecosystem on Louisiana Shelf

May 2024

Authors:
Z. George Xue, Kehui Xu, Kanchan Maiti, Cassie Glaspie, Yanda Ou, Wenqiang Zhang, Patrick O Clower, Jillian C Tupitza, Ziyan Lei

Prepared under Agreement M20AC10001
by
Louisiana State University
93 South Quad Drive
Suite 1002
Baton Rouge, LA 70803

U.S. Department of the Interior
Bureau of Ocean Energy Management
Gulf of Mexico Regional Office
New Orleans, LA

BUREAU OF OCEAN ENERGY MANAGEMENT

DISCLAIMER

Study collaboration and funding were provided by the U.S. Department of the Interior, Bureau of Ocean Energy Management (BOEM), Environmental Studies Program, Washington, DC, under Agreement Number M20AC10001 with Louisiana State University. This report has been technically reviewed by BOEM, and it has been approved for publication. The views and conclusions contained in this document are those of the authors and should not be interpreted as representing the opinions or policies of BOEM, nor does mention of trade names or commercial products constitute endorsement or recommendation for use.

REPORT AVAILABILITY

CITATION

Xue Z, Xu K, Maiti K, Glaspie C, Ou Y, Zhang W, Clower P, Tupitza J, Lei, Z. (Louisiana State University, Baton Rouge, LA). 2024. Impact of non-linear sedimentation on dredge area benthic ecosystems on the Louisiana shelf. New Orleans (LA): U.S. Department of the Interior, Bureau of Ocean Energy Management. 65 p. Agreement No.: M20AC10001. Report No.: OCS Study BOEM 2025-005.

ABOUT THE COVER

Map showing the spatial distribution of benthic ecological patterns (macrofaunal diversity and hypoxia risk), fluid mud thickness, and oil infrastructures in the Louisiana shelf. Circles denote benthic species diversity measured by Shannon diversity, while colors of the circles represent the frequency of bottom hypoxia from 1985 to 2014: red (high risk, ≥75%), orange (moderate risk, 50%–75%), and green (low risk, <50%). Fluid mud thickness (in m) is represented by bluish color. Oil infrastructures are marked by gray lines (pipelines) and "+" symbols (oil platforms).

Contents

List of Figures

List of Tables

List of Abbreviations and Acronyms

Short form	Long form
BBB	borrow area biology and biogeochemistry
BBL	bottom boundary layer
BOEM	Bureau of Ocean Energy Management
CDP	Caminada Dredge Pit
CFSv2	Climate Forecast System Version 2
COAWST	Coupled Ocean-Atmosphere-Wave-and-Sediment Transport Modeling System
CSTMS	Community Sediment Transport Modeling System
DEMS	digital elevation models
DoD	difference of depth
FM	fluid mud
HCl	hydrochloric acid
LOI	loss-on-ignition
mean_fm	mean fluid mud thickness
NCEP	National Centers for Environmental Prediction
NGOM	Northern Gulf of Mexico
NIST	National Institute of Standards and Technology
OCS	Outer Continental Shelf
PCA	principal component analysis
PCDP	Peveto Chanel Dredge Pit
RIDP	Raccoon Island Dredge Pit
ROMS	Regional Ocean Modeling System
SB	Sabine Bank
SOC	Sediment oxygen consumption
SPDP	Sandy Point Dredge Pit
spp.	species
SSBA	Ship Shoal Borrow Areas
SWAN	Simulating Waves Nearshore model
TiS	Tiger Shoal
TN	total nitrogen
TOC	total organic carbon
TrS	Trinity Shoal
WAVCIS	wave-current information system
WBL	wave boundary layer
WRF	Weather Research and Forecasting model
WSFM	wave-supported fluid mud

1. Introduction

1.1 Background and Study Purpose

Barrier islands are sandy sedimentary environments separated from the mainland by estuary or lagoon environments. The barriers protect the mainland coast and interior wetlands from meteorological and marine forcings and help to regulate estuarine conditions. In Louisiana, coastal erosion is a chronic problem (SWAN, Barras et al. 2004; Penland et al. 2005; Williams et al. 1997). Thus, there is a constant need for very large quantities (hundreds of millions of cubic meters) of sediments for coastal protection and restoration in Louisiana. Sand is needed for barrier restoration, and mixed sediment and/or mud is needed for wetland restoration. The need is likely to increase significantly in the future as sea-level rise accelerates and the frequency and/or intensity of Atlantic storms increases because of global climate change (Knutson et al. 2010; Murakami et al. 2020; Walsh et al. 2016). Though mixed and muddy sediments are most abundant in coastal Louisiana, sand is mostly limited to shoals and buried paleo river channels(Stone et al. 2004; Xu et al. 2022). A major component of the State of Louisiana's effort to manage coastal land loss is to restore degraded barrier shorelines by dredging sand resources from offshore borrow areas, which are also referred to dredge pits, and delivering to the coastal sedimentary environments.

The Bureau of Ocean Energy Management (BOEM) has allocated an estimated 198 million cubic yards of sand from the Outer Continental Shelf (OCS) for beach nourishment projects between 1995 and 2024 for the Gulf of Mexico (GOM) and the Atlantic. Approximately 66.0 million cubic yards was for Louisiana[1] . The physical changes after pit excavations can alter the water quality, planktonic and benthic communities, nekton, primary and secondary production, and microbial communities inhabiting the borrow areas. The potential changes to biological communities in dredge pits can occur due to the defaunation of sediment by the dredging process, physical changes to the water column caused by stratification, hypoxia and water quality changes within the pit, and changes in sediment size and dynamics in and around the pit (Nairn et al. 2004).

Traditional techniques using the decay of radioisotopes such as ^{234}Th, ^{7}Be, ^{210}Pb, and ^{137}Cs to estimate sedimentation rates and absolute ages of sediment layers over timescales of weeks to months (using ^{234}Th and ^{7}Be) to decades (with ^{210}Pb and ^{137}Cs), must adhere to a key assumption that the sedimentation is a steady state (linear) process (Maiti et al. 2010). While existing radionuclide studies provide valuable information on seasonal to decadal scales, the difference between short-term and long-term deposition rates implies the relative importance of episodic events. In addition, radionuclide chronology cannot quantitatively evaluate hydrodynamics' impact on sedimentation, and physical reworking introduced by waves and currents might compromise the temporal resolution and accuracy of such measurements. The realistic sedimentation environment, specifically on a relatively short time scale, is susceptible to many disturbances, such as floods, tropical cyclones and hurricanes, and cold fronts.

This study focused on examining the dynamics, biogeochemical, and ecological impacts of wave-supported fluid mud (WSFM) events within and around dredge pits on the Louisiana Shelf (Figure 1) located in the northern Gulf of Mexico (NGOM). Through comprehensive fieldwork, laboratory analyses,

---

[1] For current BOEM marine mineral statistics, see https://www.boem.gov/current-marine-minerals-statistics (as of November 19, 2024).

and numerical modeling, the study sought to assess changes in sediment transports, sediment oxygen demand, chemical gradients at the sediment-water interface, and the responses of microbial and macrobenthic communities to WSFM events. Ultimately, the findings are intended to guide coastal engineering practices and habitat restoration efforts, enhancing our understanding of benthic recovery processes and the management of fluid mud's environmental impacts.

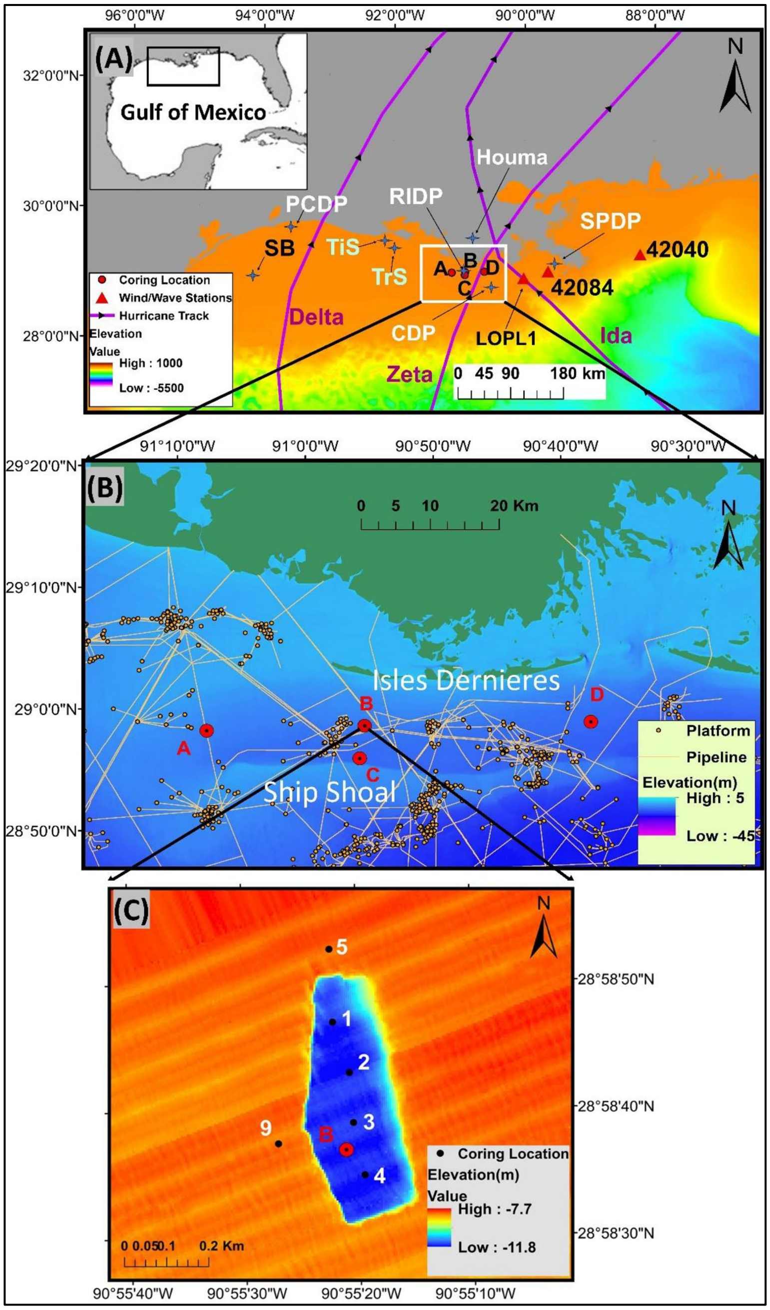

Figure 1. Study area.

Top panel: Map for multicores location and the tracks of hurricanes Delta, Zeta, and Ida. Middle panel: A zoomed-in map of top panel around the dredging pits. Bottom panel: A zoomed-in map of middle panel around site B with the locations of vibracores. Bathymetry data shown in top and middle panels were from ETOPO1. Oil platform and pipeline location data were downloaded from BOEM website. Stations A, B, C, and D are multicores and stations 1, 2, 3, 4, 5, and 9 in the bottom panel are vibracores. Only station B, 1, 2, 3, and 4 are inside the Raccoon Island pit. Bathymetric data from the Raccoon Island dredge pit were collected in August 2015 by Liu et al. (2020). On the top panel, ‘TiS’, ‘TrS’ and ‘SB’ are Tiger Shoal, Trinity Shoal, and Sabine Bank, respectively; ‘PCDP’, ‘SPDP’, ‘CDP’, and ‘RIDP’ are Peveto Chanel Dredge Pit, Sandy Point Dredge Pit, Caminada Dredge Pit, and Raccoon Island Dredge Pit, respectively. All the multicores and vibracores data were collected for this study (from (Zhang et al. 2023).

Fluid mud, an intermediate stage between consolidated deposition and diluted suspension, is a fine-grained non-Newtonian slurry characterized by high concentration (> 10 g/L) and hindered settling (Rossa and Mehta 1989; Sahin et al. 2012; Sheremet et al. 2005). Unlike classical turbidity currents supported by turbulence via gravity-driven motion, fluid mud over a mild slope (< 0.7°) is supported by ambient waves and currents and moves down-slope (Wright et al. 2001). Due to different suspension maintenance mechanisms, fluid-mud can be grouped as (1) wave-supported fluid-muds (Harris et al., 2005), (2) current-supported fluid-muds(Wang et al. 2010), and (3) wave-current-supported fluid-muds (Ma et al. 2010). Fluid mud’s importance for cross-shelf sediment transport has been reported in estuaries and continental shelves all around the world. The most direct impact of an anoxic fluid mud on the benthic ecosystem is enhanced NO_2 and N_2O concentration due to incomplete nitrification or enhanced denitrification (Abril et al. 2000). In the Atchafalaya subaqueous delta and Chenier Plain mudflats, wave activities are highly intensified due to the passages of winter cold fronts when the WSFM dispersal becomes vital and has been reported in previous studies(Allison et al. 2000; Jaramillo 2008; John T. Wells 1981; Kineke et al. 2006; Safak et al. 2010). As such, winter is treated as the ideal season for the WSFM formation in the Louisianan Shelf. During a winter cold front, the muddy top set/foreset of the subaqueous delta near the Atchafalaya Bay mouth goes through a cycle of liquefaction, erosion, and deposition with the formation of fluid mud and its consolidation (Sahin et al., 2012).

Field work was based on deployment of tripods, anchor stations, buoy stations, and collection of sediment cores have been conducted to explore WSFM dynamics in the western part of the Louisiana shelf (Denommee et al. 2018; Jaramillo et al. 2009; Kineke et al. 2006; Safak et al. 2010; Sahin et al. 2012; Sheremet et al. 2011; Sheremet and Stone 2003; Traykovski et al. 2015), whereas fluid-mud-related hydrodynamic and sediment observation methodologies in the bottom boundary layer are still limited. In addition, sampling fluid muds and measuring gravity-induced sediment flux on a large spatial scale are still challenging, and such difficulties prevent an assessment of the liquefaction, erosion, and, finally, deposition of fluid mud, let alone its impact (anoxia) on the benthic ecosystem. Numerical modeling, as an alternative method for studying WSFM, has been adapted to investigate the fluid-mud dynamics and its interaction with hydrodynamics. For instance, (Safak et al. 2010; Sahin et al. 2012) utilized a simplified uni-dimensional Bottom Boundary Layer (BBL) model and revealed that the existence of fluid mud controls turbulent kinetic energy balance and the sediment dynamics at sea floor.

Fluid-mud mobilization can impact various chemical transformations taking place in shelf sediment and can result in large gradients in many chemical species across the sediment-water interface. Such biochemical changes in the sediment can also impact the sediment microbial community as well as the benthic community (e.g., through changes in sediment oxygen demand and more pronounced hypoxia, which can lead to higher sulfate reduction in sediments resulting in increased production of H_2S, which can inhibit both denitrifying bacteria and benthic communities). The redox sequence commonly observed in sediments leads to changes in the partitioning of solutes between carrier and solution phases. Such processes can cause rapid diffusion of released species to the overlying water column or their removal onto secondary carrier phases within the sediments. When considering the area over which this can happen, fluxes from sediments can become a major source or sink in coastal chemical budgets (Fennel et al. 2006). In a highly eutrophic system like coastal Louisiana, the sediment O_2 consumption and the microbially mediated nitrogen transformation pathways are altered because of such fluid-mud events and their subsequent impact on the organic matter remineralization in the sediments. Thus, in this study, sediment core incubation has been collected and carried out both before and after fluid-mud events to understand fluid-mud-induced changes to O_2 consumption rates, organic matter remineralization rates, and associated NO_3/NO_2/NH_4 fluxes at the sediment-water interface.

Dredging can drastically change the benthic community, resulting in lower benthic abundance, biomass, and diversity that persists for years (Palmer et al. 2008). Disturbances to the benthic community, such as erosion, deposition, and low dissolved oxygen, cause the mortality of sensitive species and prevent the recruitment (settlement) of a wide variety of organisms (Diaz and Rosenberg 1995; Palmer et al. 2008; Rosenberg 1995). Thus, benthic recovery rates in recently dredge pits are often monitored using benthic infauna, which responds to changes in sedimentation, dissolved oxygen, and organic matter availability (Borja et al. 2000; Schaffner 2010).

Non-linear sedimentation likely alters benthic recovery rates and trajectories in dredge pits. Juvenile and adult macroinvertebrates can cope with 5–10 cm of rapid sediment deposition (Bolam 2011; Hinchey et al. 2006). However, recovery of the benthic community in dredged pits usually occurs due to the recruitment of larvae, which are not as mobile as adults and are likely to be smothered by rapid sedimentation events. Fluid mud may also be a stressor for the benthic community because it is not dense enough to allow organisms to migrate vertically; therefore, a layer of fluid mud interferes with respiration at the water-sediment interface (Diaz 1994). Finally, areas with high sediment deposition rates generally also have low organic matter content and less food availability for deposit feeders (Schaffner 2010). The loss of deposit feeders represents a decrease in functional diversity, which is defined as the number of roles organisms fill in each environment (in this case, based on the trophic niche) (Glaspie and Seitz 2017).

The impacts of fluid mud are not restricted to dredge pits alone; fluid mud layers flow and spread out over large areas. However, the base community before a fluid-mud event is expected to be different inside dredge pits than outside the pits. The benthic invertebrate community present before a fluid-mud event may influence the benthic fauna’s resistance and resilience to these events. It is important to understand benthic recovery in dredged pits because benthic species are often used as biotic indicators of ecosystem health (Borja et al. 2000). An examination of the relationship between fluid-mud events and benthic ecosystem recovery can inform monitoring protocols and permitting decisions in the NGOM.

1.2 Present State of Knowledge

Based on numerous studies, (Nairn et al. 2005) proposed a conceptual diagram of pit infilling and pit margin erosion processes. As the flow enters the pit, the sediment settling leads to deposition (Figure 2). As flow leaves the pit and water depth is reduced, the flow speed increases to match the ambient flow speed in the absence of the pit. The sediment load capacity of the flow at the outgoing edge is similar to the load capacity at the incoming edge based on the conservation of water mass. However, the suspended sediment concentration at the outgoing edge is less than capacity once the flow accelerates to ambient flow speed due to deposition in the pit. This results in bed erosion beyond the outgoing edge to restore sediment concentration to an equilibrium level.

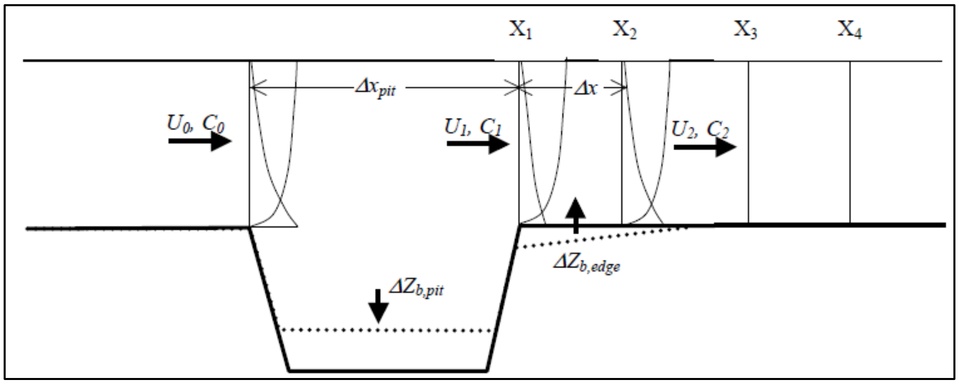

Figure 2. Pit infilling and pit margin erosion processes conceptual diagram (Nairn et al., 2005).

U is velocity, C is sediment concentration, X is distance from the pit edge, and Z is elevation change.

Recent studies revealed a considerable mismatch between observed and predicted infilling using Nairn's model. Nairn et al. (2005) predicted that it generally takes about 15 years to completely infill a dredge pit on the Louisiana shelf. From 2014 to 2017, Xu and colleagues studied physical and geological processes in three mud–capped dredge pits (report BOEM 2022-006, "An Assessment of Mud-Capped Dredge Pit Evolution on the Outer Continental Shelf of Northern Gulf of Mexico"[2], [Xu et al. 2019]). In the summer of 2015, the team collected sub-bottom CHIRP seismic profiles at Sandy Point and found a 0.5-m thick acoustically transparent layer on top of the dredge pit bed (Xu et al. 2016a), which indicates possible "fluid-mud." In the summer of 2018, Xu's group found that it took < 6 years to fill up the Raccoon Island dredge pit, much shorter than the prediction of Nairn et al. (2005). One possible explanation for such a fast infilling is the contribution from non-linear sedimentation processes. Recently, Xue's team successfully incorporated a new 3-dimensional fluid-mud module into the Regional Ocean Modeling System platform (ROMS, Haidvogel et al. 2008; Zang et al. 2020) and carried out a number of sensitivity tests. Preliminary model results indicate that after three cold fronts passed through the area in March 2016, the fluid-mud-introduced deposition could accumulate up to 6 cm in only 20 days at the Raccoon Island dredge pit, which is located between Isle Dernieres and Ship Shoal (Figure 3).

---

[2] See the report BOEM 2022-006, An Assessment of Mud-Capped Dredge Pit Evolution on the Outer Continental Shelf of Northern Gulf of Mexico here: https://espis.boem.gov/final%20reports/BOEM_2022-006.pdf

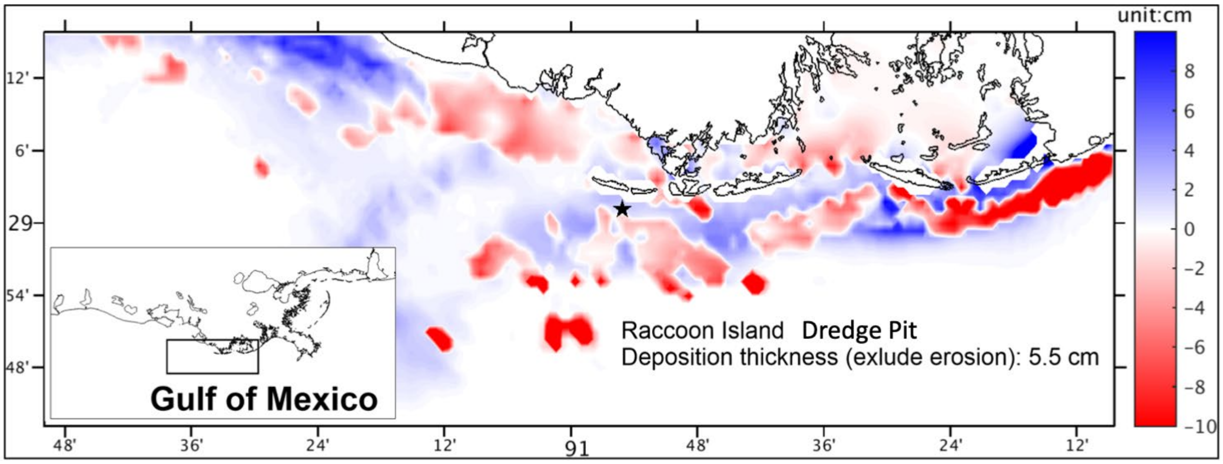

Figure 3. Simulated fluid-mud deposition (blue) and erosion (red) in March 2016.

Results are derived by a 3-D ROMS coupled hydrodynamic-sediment-fluid-mud model embedded on the COAWST modeling platform. Model results were from Zang et al. (2020). The Raccoon Island dredge pit is marked by a star.

Between 2014 and 2017, Xu, Bentley, and others were funded by BOEM through the Louisiana State University (LSU) Coastal Marine Institute program under Cooperative Agreement M14AC00023 to work on a study “Assessment of Mud-Capped Dredge Pit Evolution on the Outer Continental Shelf of Northern Gulf of Mexico” (Xu et al. 2019). The three areas in which this study focused were Peveto Channel, Raccoon Island, and Sandy Point Southeast dredge pits (Figure 4), which had been dredged in 2003, 2013, and 2012, respectively. The Sandy Point Southeast dredge pit had notable differences from the other two: (1) it was the only one from which overburden (~1.32 mcy), a layer of soil and rock that lies above a specific area of interest, was removed and disposed of nearby, and (2) the excavation in Sandy Point Southeast dredge pit (~40 ft deep) was considerably deeper than that in the Raccoon Island dredge pit (~24 ft deep) and Peveto Channel dredge pit (~40 ft deep). In 2016–2019, Xu, Bentley, and others continued to study physical and geological processes in two sandy dredge pits in Ship Shoal Borrow Areas (Agreement M16AC00018, called “SSBA”). Following that, in 2018, Xu, Xue, Maiti, and others were funded by BOEM to study water quality conditions and biogeochemical processes of these borrow areas (Xu et al. 2022), which might be stressors for fish species and benthic communities. However, to the best knowledge of the team, the benthic community and its response to fluid-mud-related sedimentation events have never been investigated. This study built upon the three above projects, leveraging resources and focusing on a potentially very important mechanism of dredge pit infilling and its impact on the benthic ecosystem. This report summarized existing and ongoing findings of infilling mud-capped dredge pits, specifically the Raccoon Island pit, followed by previous findings of water quality conditions in other mud-capped dredge pits.

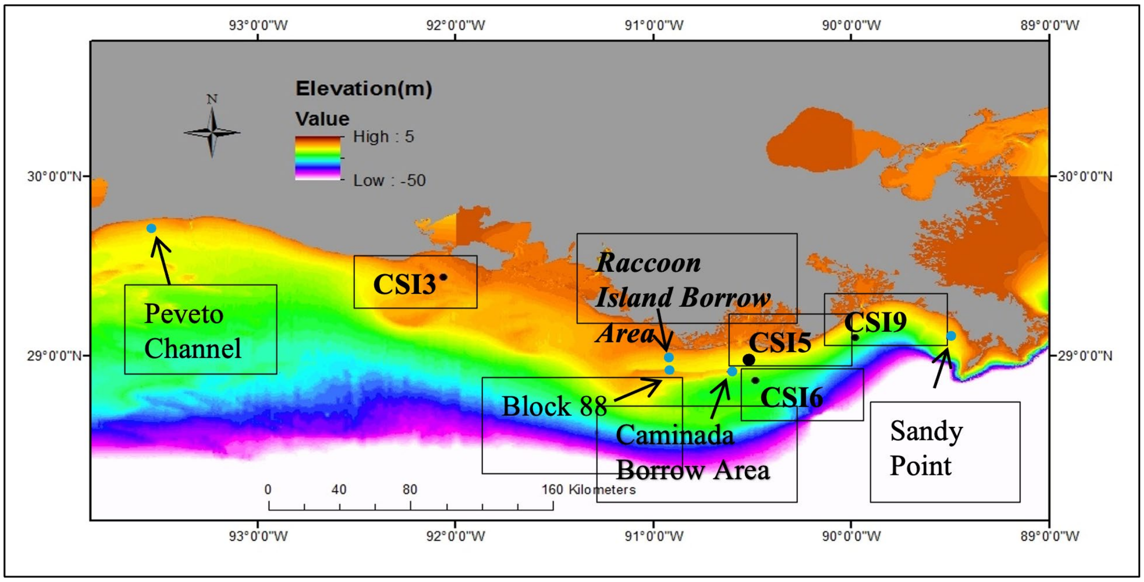

Figure 3. Locations of five past study sites and active LSU WAVCIS (wave-current information system) stations.

The past study sites are denoted by blue dots, including Peveto Channel, Raccoon Island, Sandy Point, Caminada, and Block 88 in the Ship Shoal area. Black dots are active LSU WAVCIS stations, CSI3, CSI5, CSI6 and CSI9.

The Isles Dernieres barrier island chain in central coastal Louisiana experienced some of the highest rates of erosion in the world from the 1890s to 1988 (Figure 5). The rapid degradation of these islands resulted in a decrease in the ability of the island chain to protect adjacent landward coastal marshes and swamps from the effects of storm surge, saltwater intrusion, an increased tidal prism, and frequent storm waves. Raccoon Island is the westernmost island in the Isles Dernieres chain (Broussard and Boustany 2005; Figure 5).

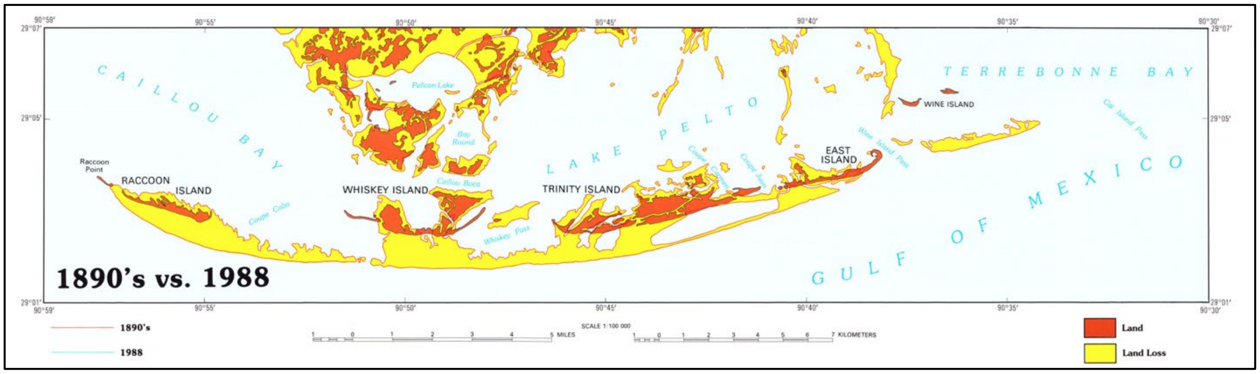

Figure 4. Shoreline change of Isles Dernieres from the 1890s to 1988 (Williams et al. 1992).

Yellow indicates land loss.

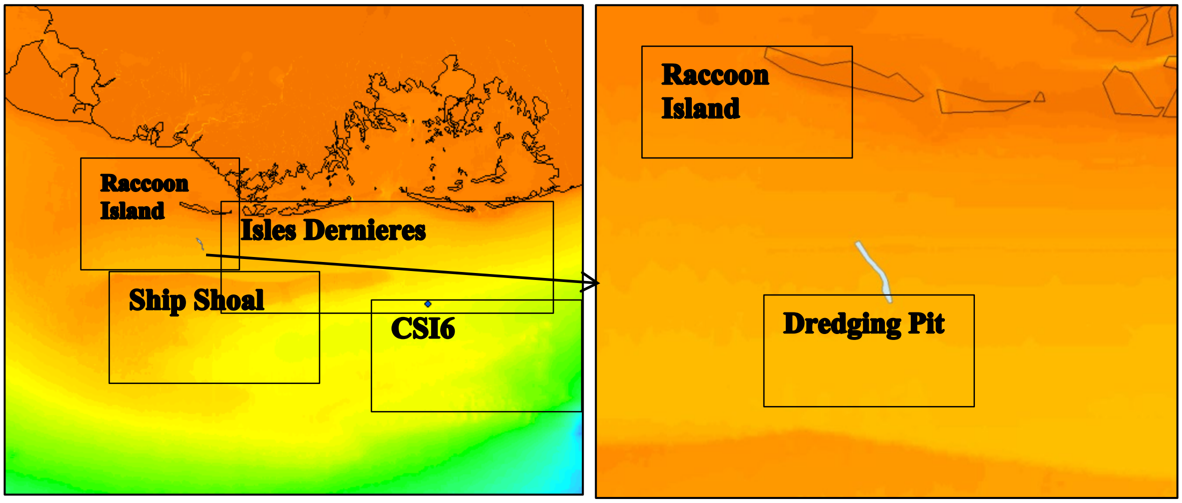

Figure 5. Locations of Isles Dernieres, Raccoon Island, and its nearby dredging pit.

See Figure 3 for location and elevation color bar.

A dredge pit was excavated in 2013 offshore Raccoon Island for the Raccoon Island Back-barrier Marsh Restoration Project. This pit is located between Raccoon Island and Ship Shoal (Figure 6). The Raccoon Island project targeted paleo-channel muddy sands with no recent muddy overburden but produced a deep pit like the Peveto Channel configuration. Previous studies by Stone (1996; 2000; 2009) and Kobashi (2009) showed that sediment transport processes on Ship Shoals include contrasting non-cohesive sand and cohesive mud transport. Muds from the Atchafalaya Bay are sometimes delivered to the Ship Shoal area and then resuspended and transported elsewhere; these “transient muds” may greatly impact the Raccoon Island dredging pit. Hydrodynamics and sediment dynamics in the Raccoon Island dredging pit are probably steered in part by the boundaries of the mainland and/or island chain in the north and Ship Shoal in the south (Figure 6).

Xu and LSU colleagues collected high-resolution subbottom seismic profiles using both low-frequency Edgetech 0512i and medium-frequency Edgetech 216 sonar systems. Two types of profiles were collected simultaneously on the port and starboard sides, respectively. Edgetech 0512i generated low-resolution but deep penetration profiles, whereas Edgetech 216 produced high-resolution but shallow penetration profiles (Figure 7 and 8; Xu et al. 2016b). This enabled us to capture large-scale geological frameworks (e.g., paleochannels) and fine-scale features such as recent sediment filling-in.

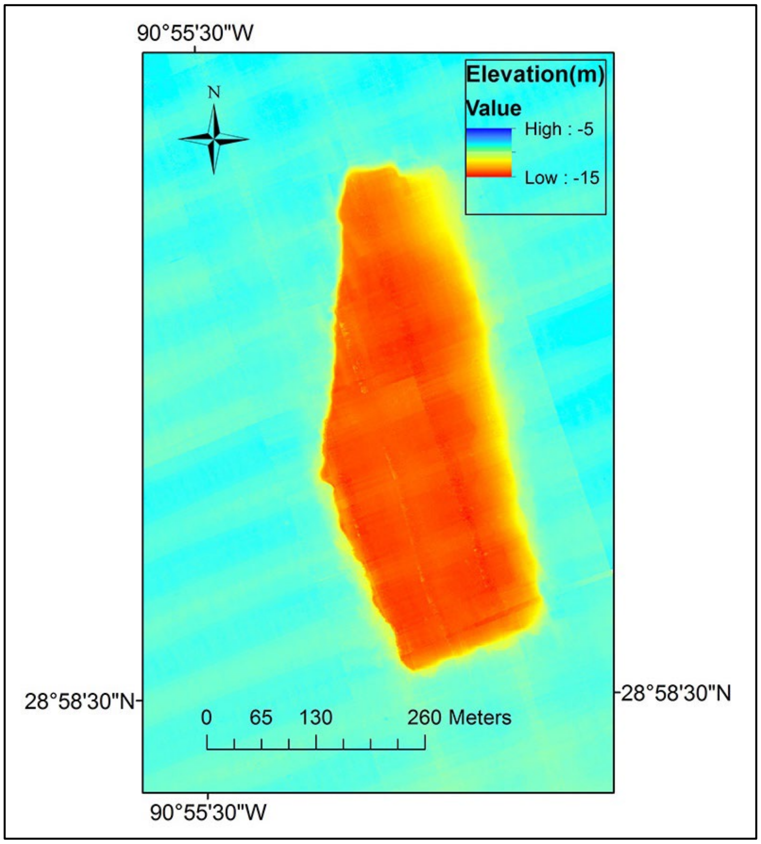

Figure 6. Bathymetry map of Raccoon Island dredge pit based on June 2015 data.

This pit is about 200 m wide and 800 m long.

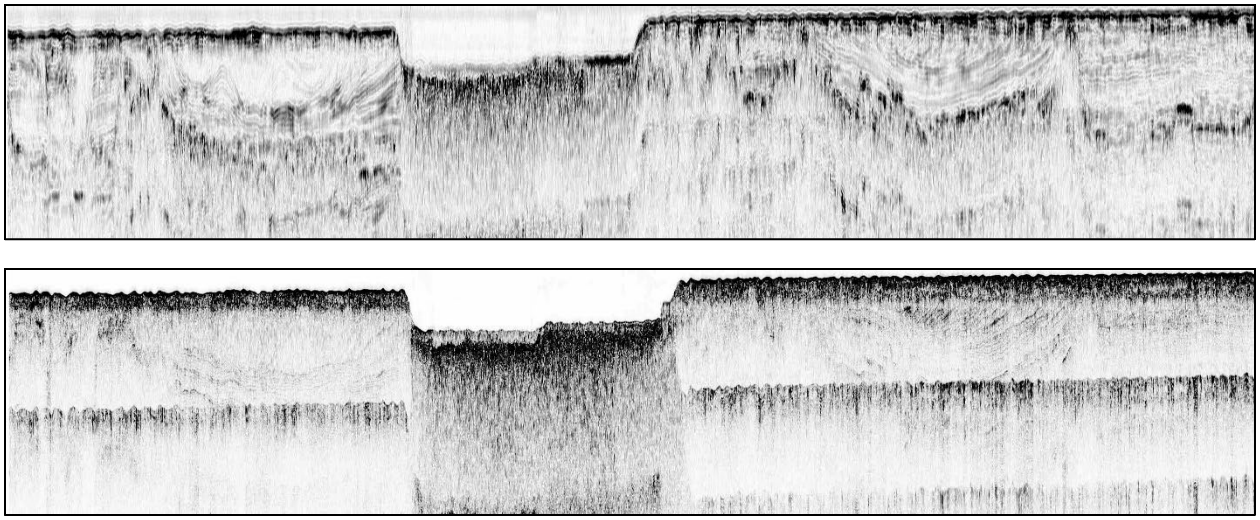

Figure 7. Examples of subbottom seismic profiles.

The upper panel shows the profiles of low-frequency Edgetech 0512. The lower panel represents the profiles of medium-frequency Edgetech 216 systems. Two profiles were collected simultaneously through the middle of the Raccoon Island dredge pit. From Xu et al. (2016b).

Sidescan sonar images were collected with subbottom and bathymetry data by Xu (2016b). Figure 9 shows two side-scan sonar images that covered the same area in the southwest corner of the Raccoon Island dredge pit but used different sides of sonar (port vs. starboard) at the same time (Xu et al. 2016b). Figure 9A captures the edge of the pit through acoustic shadow, whereas Figure 9B shows better sediment deposition inside the pit. Geophysical data indicated the dredge pit walls had undergone differential slumping, and some failures morphologically resemble features observed along the muddy Mississippi River Delta Front at water depths of 20–100 m, including bowl-shaped collapse depressions and retrogressive stair-stepped slides(Obelcz et al. 2016). In addition, radionuclide analyses showed 26–50 cm deep of ^{7}Be activity in Raccoon Island dredge pits. This study revealed a level of 0.5 to 1 m/yr infilling rate, which is higher than a few cm/yr of accumulation of the Mississippi and Atchafalaya River mouths and much higher than mm/yr of accumulation on the middle Louisiana shelf. Possible contributions from non-linear sedimentation, such as fluid mud, have not been investigated yet. Regardless of the source, the dredge pits are accumulating a record of sediment that would not be recorded on the shelf otherwise, and collapses of pit walls cannot totally explain the whole depositional process(O'Connor et al. 2016; Xu et al. 2016b).

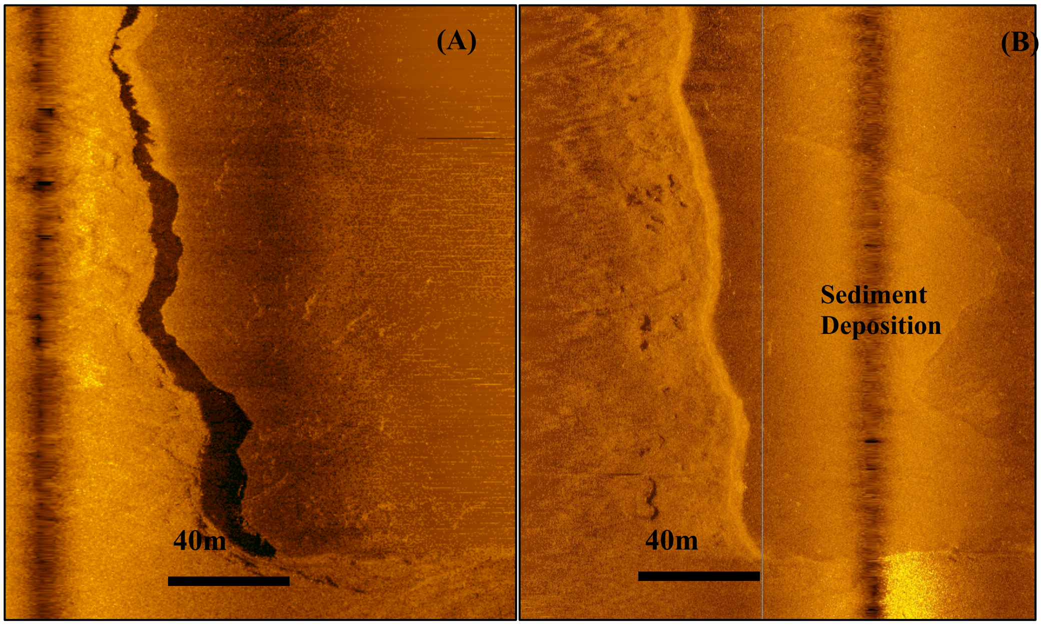

Figure 8. Sidescan sonar images collected in the southwest corner of the Raccoon Island dredge pit.

Acoustic shadows show a clear pit wall edge on the left panel (A). A pile of sediment deposits is found on the right panel (B). From Xu et al. (2016).

In the summer of 2015, Xu and Bentley deployed a tripod and collected sediment cores inside this pit. One month later, when they retrieved the tripod, they found dark-black sediment and/or organic matter coating the entire tripod and all the sensors, with a strong sulfide smell, which was indicative of a low oxygen condition (Xu et al. 2016b; Figure 10), similar to the characteristics observed in sediment cores (sulfidic, no living macrofauna, and black sediments at the sediment-water interface). Later, the laser grain size data of these sediment samples confirmed a very fine-grained texture. Xu and Bentley also collected sub-bottom CHIRP seismic profiles using multiple Edgetech systems and found a 0.5-m thick acoustically transparent layer sitting on the dredge pit bed (Xu et al. 2016b; Figure 10), which was indicative of possible fluid-mud and a very sluggish environment. The top of this fluid-mud layer is generally defined as a lutocline, which is a depth at which sediment concentration increases suddenly up to 10s g/L. This sudden change was also detected as a secondary water-sediment interface by the CHIRP system (Figure 11).

Figure 9. Pictures of instrumented tripod.

Top left panel (A) represents the tripod before deployment; top right panel (B) the tripod after retrieval; bottom panel (C) the zoom-in picture of mud and organic matter attached to a leg of the tripod after retrieval in the summer of 2015. From Xu et al. (2016b).

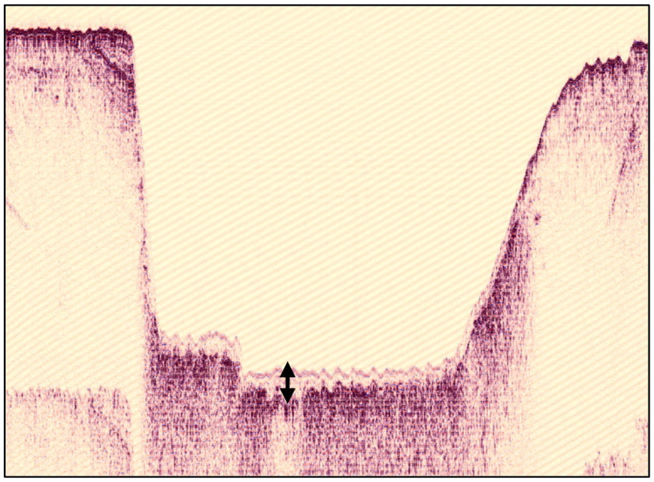

Figure 10. Sub-bottom seismic profile collected at Sandy Point dredge pit.

Note that the 0.5-m thick acoustically transparent layer is sitting on the dredge pit bed (black double arrow). This layer is between primary (bottom) and secondary (top) water-sediment interfaces. From Xu et al. (2016b).

Water quality data was also collected for another BOEM study, “Development of a Monitoring Program for Water Quality and Biogeochemical Processes of Louisiana Sediment Borrow Areas”, or “BBB”, under Cooperative Agreement M17AC00019 (Xu et al. 2022). On May 8 and 9, 2018, a Sea-Bird Coastal

HydroCAT-EP was used to collect profiling data inside and outside the Caminada dredge pit. Inside the pit, hypoxia was found at two stations (Figure 12).

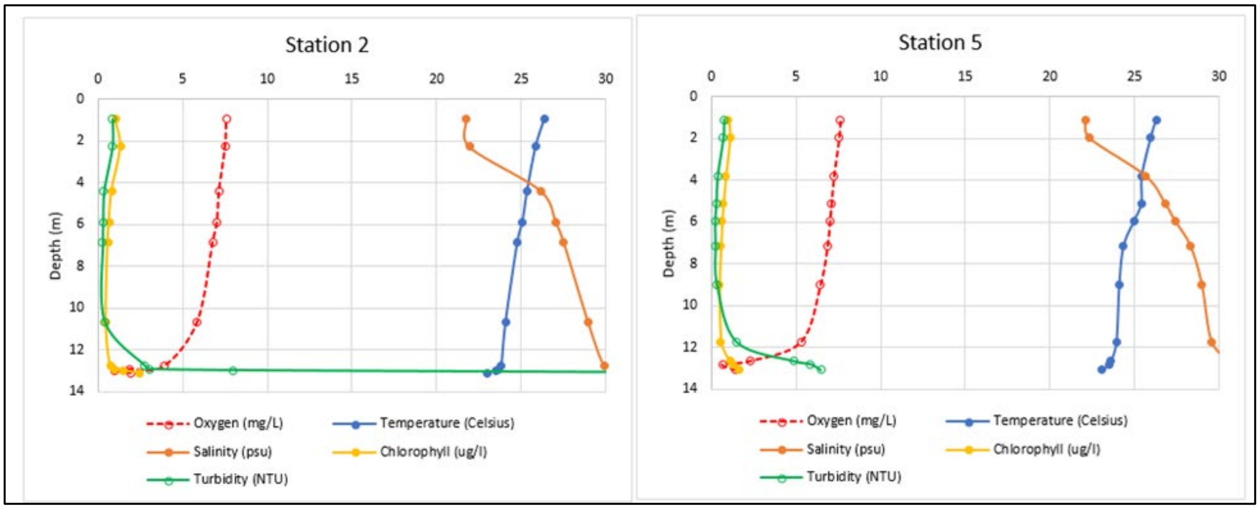

Figure 11. HydroCAT profiling data collected at two stations inside the Caminada dredge pit.

From the BBB report seeing Xu et al., 2022. Note the hypoxia at both locations.

2. Goals and Objectives

2.1 An Overview of Study Goals

Previous studies had revealed a faster-than-expected infilling rate at mud-capped dredge pits and possible fluid mud in the bottom boundary layer. In addition, the water quality in the dredge pit exhibited contrasting biogeochemical characteristics compared with shelf waters. As a result, a new study was proposed and carried out here to investigate sedimentation and benthic ecology in the Raccoon Island dredge pit and adjacent waters (Figure 1) using combined field observations, coring, data synthesis, and modeling methods. This study aimed to comprehensively understand the WSFM process on the OCS and its contribution to dredge pit infilling, and its impact on benthic ecology. This was the first BOEM study specifically targeting fluid-mud and benthic ecology.

The detailed objectives of this study were to:

(1) collect new geophysical data, sediment cores, and benthic fauna during the summer of 2020, about seven years after dredging, to build the frame of reference for sediment and benthic ecology;

(2) collect new sediment and benthic fauna at Raccoon Island and adjacent shelf waters in the spring, fall, and winter of 2021 (to capture impacts of and recovery from fluid-mud events);

(3) develop statistical models describing the impacts of both dredging and fluid-mud on benthic community composition, diversity, and production, including changes over time (recovery from fluid-mud events);

(4) further develop a new 3-dimensional fluid-mud model for the nGoM shelf; use collected data to further calibrate the model and evaluate model performance;

(5) generate probability maps for WSFM using the correlation among fluid-mud, wave, current, sediment, and other variables;

(6) determine linear sedimentation rates associated with fluid-mud events;

(7) quantify changes in sediment O_2 consumption, organic matter remineralization and NO_3, NO_2, NH_4 associated with fluid-mud events;

(8) identify impacts of fluid-mud on benthic community composition using existing benthic ecological data/samples in the OCS region, benthic community composition data from the proposed study, and fluid-mud probability maps;

(9) overlay fluid-mud distribution and benthic community composition maps with locations of dredge pits and oil/gas platforms and provide recommendations for BOEM's decision making ability (e.g., infilling rate, pit impact to surrounding benthic ecosystems, recovery trajectories, monitoring recommendations).

2.2. Hypotheses and Research Questions

The objectives outlined above were set forth to help answer the following research questions.

H1: Cold front wave mobilization can greatly increase the sediment infilling rates of dredge pits, which are much higher than the commonly used predictions of Nairn et al. (2005);

H2: Shelf sediment's response to the fluid-mud process is different in and outside the already-filled pit, with more mud deposited over the pit because of its depressed surface;

Methods to test H1 and H2: Sediment cores were collected in and outside the dredge pit site in the summer of Year 1 to build the frame of reference for non-fluid mud conditions. This sampling was repeated in Year 1 (Spring) and Year 2 (Fall and Winter) to capture evidence of fluid-mud-induced sedimentation. Local chronology based on the collected sediment cores was built using radionuclide techniques. Data was collected to calibrate a 3-dimensional numerical model for current conditions (year 2020-2021) and then forecast previous conditions.

H3: WSFM is a significant stressor to benthic ecology, and the benthic community's composition and response to fluid-mud events are different inside and outside the dredge pit;

Methods to test H3: Whole core lab incubation experiments were performed to determine changes in sediment O_2 consumption, organic matter remineralization, and NO_3, NO_2, and NH_4 using the newly collected sediment core. Benthic macrofauna (> 1 mm) and meiofauna (> 500 µm) from box core samples were collected. This study also determined the benthic community composition inside and outside the dredge pit, both in the summer (baseline) and in other seasons when fluid-mud events typically occur (spring, fall, winter). Benthic species diversity, functional diversity, abundance, biomass, and benthic secondary production (rate of biomass generation by benthic heterotrophic organisms) were calculated and analyzed for treatment differences.

H4: On the shelf scale, areas with a high probability of fluid-mud events have low benthic productivity, and vice versa.

Methods to test H4: To address this hypothesis, a probability map of fluid-mud distribution using model-simulated physical and sediment variables was built. Benthic community composition, biomass, and secondary production were analyzed by compiling existing ecological data for the larger OCS region, including previously unprocessed shelf benthic samples from 2012 to 2014. These analyses were integrated with fluid-mud probability maps to assess variations in benthic communities across areas with high and low fluid-mud probabilities.

3. Method

3.1 Field Data Acquisition

3.1.1 Vibracores, Multicores, and Box cores

A total of three types of coring methods were used: vibracores, multocores, and GOMEX box cores. Vibracore effort was funded by NSF and USACE and some details are in Zhang (2023). The collections and analyses of multicores and GOMEX box cores were funded by this BOEM project.

Several vibracores and multicores were collected from stations around the Raccoon Island dredge pit (Figure 1). The vibracores were collected using the R/V *Coastal Profiler*, equipped with 5-meter-long aluminum core barrels (Figure 1; Table 1), which were then capped, sealed, and transported to the lab for further analysis (Liu et al. 2020). Multicores and box cores were collected aboard the R/V *Acadiana*, utilizing an Ocean Instruments MC400 multicorer and others, designed to minimize disturbance to the sediment-water interface, ensuring the integrity of the samples for accurate sedimentological analysis.

Multicores were collected at four stations (A, B, C, and D) in cruises 1 (March 12, 2021), 2 (July 7, 2021), 3 (November 20, 2021), and 4 (March 5, 2022), respectively. In this BOEM project, the naming of the multicore stations is a combination of a short project name (NLS – Non-Linear Sedimentation, this BOEM project), cruise number (1–4), and station (A). For instance, NLS3D is a multicore collected during cruise #3 at station D for the Non-Linear Sedimentation project.

Table 1a. Vibracores: sediment cores collected during multiple field cruises

Location	Core #	Date of Collection	Longitude (degree)	Latitude (degree)	Depth below sea surface (m)	Core length (m)
1	**RI1**	8/19/2020	-91.0089	29.1781	12.1	1.97
2	**RI2**	8/19/2020	-91.0139	29.1628	11.8	2.63
3	**RI3**	8/19/2020	-91.0108	29.1456	11.5	3.01
4	**RI4**	8/19/2020	-91.0103	29.1261	10.9	3.31
5	**RI5**	8/19/2020	-91.0317	29.2122	10.6	3.78
6	**RI9**	8/19/2020	-91.0247	29.2278	10.2	3.28

See Figure 14 for the coring location. RI is Raccoon Island dredge pit and nearby area, NLS is short name of project “non-linear sedimentation”. Coordinates are in NAD83 geographic coordinate system (from Zhang et al., 2023).

Table 1b. Multicores: sediment cores collected during multiple field cruises

Location	Core #	Date of Collection	Longitude (degree)	Latitude (degree)	Depth below sea surface (m)	Core length (m)
A	**NLSA**	3/12/2021	-91.1286	28.9702	7.9	0.2
A	**NLSA**	7/7/2021	-91.1286	28.9702	7.9	0.2
A	**NLSA**	11/20/2021	-91.1286	28.9702	7.9	0.2
A	**NLSA**	3/5/2022	-91.1286	28.9702	7.9	0.2
B	**NLSB**	Same above	-90.9226	28.9769	8.3	0.16~0.2
C	**NLSC**	Same above	-90.9289	28.93237	10.1	0.12~0.2
D	**NLSD**	Same above	-90.6274	28.9824	9.8	0.14~0.2

Vibracores were logged using a Geotek Multi-Sensor Core Logger to measure bulk density and porosity at fine-scale intervals via gamma ray attenuation. This method allowed for precise characterization of the sediment layers, critical for assessing changes in sediment deposition over time (Heiri et al. 2001). Each vibracore was then split lengthwise, and detailed sedimentological features were recorded, providing data on the textural and compositional changes within the sediment column.

At every NLS station, multicores were collected to be analyzed for total organic carbon percent (%TOC) content at 1–2 cm depth intervals and for ^{7}Be. Approximately 20 liters of bottom water were also collected for use in core incubation experiments from each station.

Benthic macrofauna was obtained from GOMEX box cores collected at one station inside the dredge pit and three locations outside the dredge pit in spring, summer, and fall 2021 and in spring 2022. Benthic meiofauna were collected at all stations (Figure 1) in summer and fall 2021 and in spring 2022. A GOMEX box corer was used to collect sediment at each station. For the enumeration of macrofauna, three 10-cm diameter cores were collected from the box core to 10 cm depth. For the enumeration of meiofauna, three 2.6 cm diameter cores were collected from the box core to 5 cm depth. The three replicate 10-cm diameter cores were rinsed in the field with seawater on a 1-cm sieve for macrofauna. The three replicate 2.6-cm cores were rinsed in the field on a 0.5-mm sieve for meiofauna. Macrofauna samples were placed in a plastic bag, kept on ice for transport, and then frozen. Meiofauna samples were fixed in 10% buffered formaldehyde solution with rose bengal stain for at least 48 hours, after which they were transferred to 70% ethanol for storage.

3.1.2 Legacy Samples for Macrofauna

Legacy samples from August and October 2013 were obtained from Carey Gelpi. Samples from 2013 were obtained either frozen or stored in 70% ethanol. Environmental data were also obtained for each sample, including temperature, salinity, and dissolved oxygen. A total of 63 samples from 2013 were used for this project. A category representing the risk of hypoxia exposure (low, moderate, high) was assigned to each sample based on the frequency of observed hypoxia from the annual hypoxia mapping cruise. These were determined from the frequency of hypoxia (bottom dissolved oxygen below 2 mg/L) at cruise stations from 1985 to 2014, with high risk equal to hypoxia frequency of 75% or greater, moderate risk equal to hypoxia frequency of 50–75%, and low risk equal to hypoxia frequency below 50%[3]. The annual mean fluid mud layer thickness (m) was extracted from the model output from the Xue lab for each sample location.

3.1.3 Geophysical Survey

The Raccoon Island dredge pit was surveyed in June 2015, August 2018, and August 2021 using a full suite of high-resolution geophysical instruments, including interferometric sonar for swath bathymetry, sidescan sonar, and chirp subbottom profiler. Some results of June 2015 survey can be found in Xu et al. (2022, final report for BOEM project M14AC00023) as well as (Liu et al. 2020). An Edgetech 4600 swath bathymetry and sidescan sonar system was used to collect data with a swath width of up to 10 times the water depth. The swath sonar frequency is 540 kHz, and the depth range below the transducer is ~50m. The 4600 system produces real-time high-resolution three-dimensional maps of the seafloor while providing co-registered simultaneous side scan and bathymetric data. Seafloor features, such as pit edges, failure scarps, and bedforms as small as 10-20 cm, can be imaged. The Edgetech 2000 DSS combined side-scan sonar & sub-bottom profiler system was used to collect CHIRP seismic profiles using a range of frequency of 2–16 kHz and side-scan data using simultaneous frequencies at both 300 and 600 kHz. The 2000 DSS system's sub-bottom profiles can reveal erosional and depositional structures with a vertical resolution of 6–10cm and a 60-m penetration depth on the muddy sea floor. An Edgetech 0512i subbottom profiler was used for the collection of subbottom profiles at a frequency of 0.5–4.5 kHz. Subbottom data collected in 2015 used both 2000 DSS system and Edgetech 0512i system, while subbottom data collected in 2018 and 2021 used only Edgetech 0512i system. Moreover, Edgetech 4600 swath bathymetry and Sidescan were used in all three geophysical data acquisition. The R/V *Coastal Profiler* from the LSU Coastal Studies Institute was used for all fieldwork. The average vessel speed during all the data acquisition was 4–6 knots. The bathymetry and sidescan acquisition device were pole-mounted and fixed from a bowsprit ahead of the vessel. The sub-bottom profiler was towed off the port side of the vessel about 0.5 m below the sea surface.

All geophysical data from the 2021 survey were combined with previous surveys performed in 2015 and 2018 by Haoran Liu. These surveys utilized various single beam echosounders and varying line spacings, ranging from 15 m to 30 m, for the surveys that provided full coverage. The total number of all surveys was 3, with each survey varying in acquisition method and coverage. Sonar data were processed using Caris HIPS/SIPS and then exported to ArcMap to create Digital Elevation Models (DEMs), which were then used to analyze slope, Difference of Depth (DoD), volume changes, and surface morphology. Subbottom profiler data were processed using Sioseis, Kingdom Suite, and Fledermaus. Detailed geophysical methods can be found in Obelcz et al. (2018) and Liu et al. (2020) . In order to acquire an estimate of uncertainty for the DoDs, the "fixed reference uncertainty" was calculated, following the methods detailed in Schimel et al. (2015).

---

[3] For information and data about the Gulf of Mexico hypoxic zone, see the EPA webs site at https://www.epa.gov/ms-htf/northern-gulf-mexico-hypoxic-zone

3.2 Laboratory Analysis

3.2.1 Sedimentological Analysis

Sedimentological analyses were comprehensively conducted using a variety of techniques. The grain size was determined through laser diffraction using a Beckman-Coulter particle size analyzer, which accommodates a broad size range (0.02 to 2000 µm), essential for detailed sediment profiling. The preparation involved mixing wet samples with hydrogen peroxide and heating them to digest organic matter, followed by sonication for uniform distribution before measurement. Organic matter and carbonate content were quantitatively analyzed via loss-on-ignition (LOI); samples were dried and then combusted at two temperatures: 550°C for organic matter and 950°C for carbonates to ascertain their respective percentages. Additionally, advanced statistical methods such as paired t-tests and correlation coefficients were employed to evaluate the relationship between grain size and organic matter across different seasons and locations, providing insights into temporal and spatial sediment dynamics.

3.2.2 Incubation Experiments

The core incubation experiment was started within 24 hours of sample collection. A temperature-controlled water bath was adjusted to the ambient water temperature recorded in the field; the incubations were performed at 20°C while only the July 2021 incubation was performed at 28°C. The overlying water column of each core was replaced with site-specific water that had been bubbled to oxygen saturation. Each core was then capped without any headspace using custom PVC caps fitted with two O-rings (to keep the core airtight) and stirrers and then submerged into the temperature-controlled water bath (Upreti et al. 2019). Each core tube was attached to the water reservoir to allow for gravity-driven replacement of water inside the core tube when the sampling ports were opened to collect water samples. The water bath with sediment cores was covered to prevent primary production and left to sit for an hour to allow the sediment cores to acclimate before the first samples were collected.

Samples were collected every four hours thereafter until oxygen levels became anoxic or reached 24 hours. Water samples were collected only after discarding the first ~10ml of dead volume in the tube, and then sampling vials were filled from the bottom and allowed to overflow. Dissolved oxygen concentrations inside the cores were monitored every sampling period using a Presens Microx 4 O2 sensor. Appropriate volume collection was carried out on samples from each time point and utilized to calculate fluxes (Ghaisas et al. 2019). O2 consumption was used to determine how fluid mud events may affect respiration.

3.2.3 Total Organic Carbon and Total Nitrogen Measurements

Total organic carbon (TOC%) was determined using a sediment core from each station during each sampling period. This core was sliced into 1 cm intervals for the top 6 cm of the core and then was subsampled, weighed, and then dried at ~60°C. Dried subsamples were ground using a mortar and pestle and homogenized through a 125-µm filter. Approximately 20 mg of each sample was placed into open Costech silver capsules and placed in a vacuum glass desiccator to fumigate with 12N hydrochloric acid (HCl) for 12 hours to remove inorganic carbon (Hedges and Stern 1984). Upon completion, samples were then repacked into tin capsules to ensure no loss of sample and analyzed in a Costech 1040 CHNOS Elemental Combustion system following the standard EPA method 440.0 (Zimmermann et al. 1997).

3.2.4 Radionuclide Analysis

Aliquots of finely ground dry sediments (5–9 g) were placed into counting vials of known geometry and measured ^{7}Be by direct gamma counting using two high-purity germanium well detectors. The detector efficiencies were determined using EPA standards and spiked with a National Institute of Standards and Technology (NIST) traceable mixed gamma liquid standard from Analytics™, Inc. All activities were corrected for decay to the midpoint of sample collection. ^{7}Be activity was measured by its emission at 477 keV. The short half-life of ^{7}Be (53.3 days) and its particle-reactive nature allowed it to be used as chronological markers to determine recent sedimentation events and expound on how these hypothesized events affected benthic respiration. ^{7}Be has successfully been used as a tracer since the late 1990s to identify recent and seasonal sedimentation and erosion events (Mullenbach and Nittrouer 2000; Palinkas et al. 2005; Sommerfield et al. 1999; Wilson et al. 2003).

3.2.5 Benthic Macrofauna

All samples were rinsed in the lab over a 0.5-mm sieve with fresh water, and benthic organisms were picked out of the substrate. Using an optical compound microscope, organisms were identified to the lowest taxonomic level, usually species. Samples from 2013 are reported by the family. Estimation of biomass was attempted by drying samples in a drying oven at 60° C for 48 hours, but due to the small size of the organisms and the low number in each sample, biomass (dry weight) was generally less than 0.001 g, the detection limit of the balance. Biomass determination was abandoned.

Benthic infaunal community composition was analyzed using the vegan package in R statistical software. For data collected at the Raccoon Island dredge pit in 2021 and 2022, a (PERmutational Multivariate ANalysis of VAriance) PERMANOVA was used to examine the impact of site (four levels, categorical), season (four levels for macrofauna, three levels for meiofauna, categorical), and the interaction between site and season on Bray-Curtis dissimilarity matrices of square-root transformed abundance data. For offshore data collected in 2013, a PERMANOVA was used to examine the impact of temperature (degrees C), salinity (PSU), dissolved oxygen (mg/L), mean fluid mud layer thickness (m), and hypoxia frequency (three levels, categorical) on Bray-Curtis dissimilarity matrices of square-root transformed abundance data. All explanatory variables were examined for collinearity, and no two variables exhibited a Pearson correlation coefficient greater than 0.6. When a significant interaction involving a categorical variable was present, the data were partitioned by the categorical variable. Multiple PERMANOVAs were run to allow for interpretation of the interaction effect. A principal component analysis (PCA) was run to complement each PERMANOVA. Vectors representing the taxonomic group that most closely aligned with the PCA axes were included in the PCA plot, as well as vectors indicating the correlation between the explanatory variables and the PCA axes.

3.3 Numerical Modeling

3.3.1 Coupled Ocean-Atmosphere-Wave-and-Sediment Transport Modeling System

Numerical modeling efforts were built upon the Coupled Ocean-Atmosphere-Wave-and-Sediment Transport Modeling System (COAWST, Warner et al. 2008; 2010), an open-source community modeling system incorporating three state-of-the-art numerical models: 1) the Weather Research and Forecasting model (WRF, Skamarock et al. 2008, 2) the (ROMS, Haidvogel et al. 2008, and 3; Shchepetkin and McWilliams 2005) the Simulating Waves Nearshore model (SWAN, Booij et al. 1999). Online coupling between ROMS and SWAN was activated to support simulations of both current-induced sediment transport and wave-supported fluid mud behaviors. ROMS is a three-dimensional, free surface terrain following an oceanic model that solves Reynolds-Averaged Navier-Stokes equations based on the hydrostatic and Boussinesq assumptions (Haidvogel et al. 2008), while SWAN was designed for simulations of wind wave and swell behaviors in shallow waters. The COAWST platform couples these models utilizing the Model Coupling Toolkit (Larson et al. 2005), which supports variable exchange between ROMS and SWAN. ROMS sends water depth, water level, and barotropic (constant with depth) current speed as input parameters to SWAN and receives the computed output parameters (such as wave direction, wavelength, significant wave height, wave energy dissipation rate, and bottom orbital velocity) from SWAN to estimate the influence of waves to the momentum at the bottom boundary layers, as well as to estimate surface roughness, and wave breaking-induced turbulent energy injection. A wave-current BBL model (Madsen 1995) was used to simulate bottom shear stress which is a function of bottom shear stresses based on pure currents (provided by ROMS) and pure waves (provided by SWAN) (Warner et al. 2008). The sediment modeling component embedded in the ROMS is discussed in the next section.

3.3.2 Community Sediment Transport Modeling System and WSFM

The Community Sediment Transport Modeling System (CSTMS, Sherwood et al. 2018; Warner et al. 2008) is an in-house sediment model or module component coupled with ROMS at the COAWST platform and has been widely used to investigate sediment transport, stratigraphy, and geomorphology in coastal regions (Moriarty et al. 2014; 2015; Xu et al. 2011; Xu et al. 2016a; Xue et al. 2012; Zang et al. 2018; Zeng et al. 2015). CSTMS (Figure 13) simulates the dynamics of both cohesive (mud) and noncohesive (sand) sediment classes, including transport, erosion, and deposition processes. Sediment erosion flux was estimated following Ariathurai and Arulanandan's (1978) method:

$$E = E_0(1-\phi)\left(\frac{\tau_{cw}-\tau_{cri}}{\tau_{cw}}\right) \quad (1)$$

where E_0, τ_{cw}, and τ_{cri} represent erosion rate, bottom shear stress, and critical shear stress, respectively. The porosity (ϕ) was set to 0.5 for all sediment layers, while critical shear stress and settling velocity of the cohesive sediment were set to 0.07 Pa and 0.1 mm/s, respectively (Xu et al. 2016a).

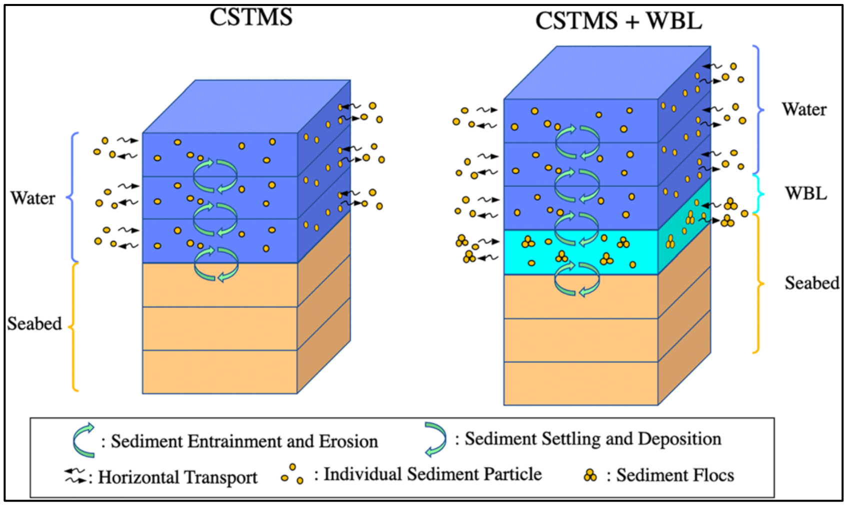

Figure 12. Diagram of original Community Sediment Transport Modeling System (CSTMS; left panel) and updated CSTMS model with wave boundary layer (WBL; right panel) to represent WSFM.

Credit: Zang et al (2020).

The wave boundary layer (WBL) plays an important role in offshore sediment transport and material exchange between the seafloor and overlying water, especially during strong wave events (Harris et al. 2005; Jaramillo 2008; Jaramillo et al. 2009; Wright and Friedrichs 2006) A newly developed WSFM module incorporates the WBL between the ROMS bottommost water column layer and the top sediment bed layer (Figure 13). As only one model layer is incorporated to represent the WBL, depth-averaged sediment concentration and momentum are resolved in WSFM. The thickness (δ_w) of WBL, which is also referred to fluid mud thickness, is estimated by the ratio of wave orbital velocity (u_w), and wave frequency (ω), i.e., $\delta_w = \frac{u_w}{\omega}$, to account for stratification between WSFM and bottom water layer (Harris et al. 2003). Different from the original CSTMS model, in WSFM, downward sediment settling flux from the bottommost water layer enters the WBL instead of the seabed. Similarly, upward suspended sediment flux into the bottom water layer comes from the WBL instead of the seabed. Eddy viscosity varying as gradient Richardson number is used to estimate the upward sediment flux, enabling the WSFM to consider stratification's impacts on fluid mud dynamics (E_wbl; Harris et al. 2003; Munk and Anderson 1948; Rossa and Mehta 1989). Sediment exchange between the seabed and the WBL is determined by the sediment erosion flux (E) and settling flux (D). Net erosion or deposition within a certain time elapse (Δt) is determined by the combined effects of these fluxes and can be parameterized as follows (Harris and Wiberg 2002):

$$E - D = (c_{eq} - c_{s,wbl})w_{s,wbl}\Delta t \quad (2)$$

where c_{eq} and $c_{s,wbl}$ denote the equilibrium sediment concentration (Smith and McLean 1977) and sediment concentration in the WBL, respectively. The $w_{s,wbl}$ is sediment settling velocity in the WBL. The given sediment erosion and deposition algorithm is different from Equation 1 used in the original CSTMS (Warner et al. 2008). The WSFM implements a linearized Chezy equation that accounts for the velocities at both the WBL and the bottom water layer with a drag coefficient of 0.004 (Wright et al. 2001) to simulate the momentum in WBL and WSFM-induced horizontal sediment flux. The governing equation of WSFM flux considering settling, resuspension, diffusion, and horizontal advection can be described as:

$$\frac{\partial(\delta_w c_{s,wbl})}{\partial t} = w_{s,water}c_{s,water} + w_{s,wbl}\left(c_{eq} - c_{s,wbl}\right) + E_{wbl} + \frac{\partial Q_{x,wbl}}{\partial x} + \frac{\partial Q_{y,wbl}}{\partial y} \quad (3)$$

where $Q_{x,wbl} = c_{s,wbl}u_{wbl}\delta_w$ and $Q_{y,wbl} = c_{s,wbl}v_{wbl}\delta_w$ are the horizontal advection of WSFM-induced sediment fluxes in x- and y-directions, respectively. A 2-dimensional Lax-Wendroff method, an explicit second-order scheme both spatially and temporally, is applied to solve this equation.

3.3.3 Model Adaptation to the Northern Gulf of Mexico

A coupled ROMS and SWAN model with the updated sediment module (CSTMS+WBL) in ROMS was applied (Table 2) to the NGOM (Figure 14) to investigate fluid mud dynamics over the year 2021. This model had been successfully adapted to this region for fluid mud simulations in March 2016 by Zang et al. (2020), where impacts of cold fronts on sediment dynamics were demonstrated. For the ROMS model, major detailed setups and parameterizations applied in this project followed the ones applied in Zang et al. (2020) including domain coverage, resolutions (1 km in horizontal dimensions and 24 vertical stretched terrain-following layers), and baroclinic time step (1 s), etc. However, more river point sources were introduced considering the impacts of the Mississippi River in this study. Time-varying river discharges, fluvial sediment concentration, temperature, and salinity were derived from the U.S. Geological Survey (USGS) river gauges[4] and were transported to computational cells via the predefined river point sources (Figure 14). Atmospheric forcings, including surface wind velocity at 10 m height above sea level, net longwave radiation flux, net shortwave radiation flux, precipitation rate, air temperature 2 m above sea level, sea surface air pressure, and relative humidity 2 m above sea level, were derived from Climate Forecast System Version 2 (CFSv2) six-hourly products (Saha et al. 2014) provided by the National Centers for Environmental Prediction (NCEP) with a horizontal resolution of ~22 km. Initial conditions and open boundary forcings (e.g., sea-level, barotropic, and baroclinic current velocity, temperature, and salinity) were interpolated from hindcast results of a parent model–the GOM model

---

[4] See the USGS Water Data for the Nation at http://nwis.waterdata.usgs.gov

developed by (Zang et al. 2019) (also see another BOEM-supported work by Ou and Xue (2024) for another model application). The parent model has a horizontal resolution of 5 km and 36 vertical sigma layers. Mixed radiation-nudging boundary conditions (Orlanski 1976) were applied to the temperature, salinity, and 3-dimensional (baroclinic) current velocity components, while boundary conditions for the water level and 2-dimensional (barotropic) current velocity followed the (Chapman 1985) implicit and the (Flather 1976) schemes, respectively.

Within the model, one cohesive (mud) and one noncohesive (sand) sediment class were specified in the CSTMS+WBL modules. Radiation horizontal boundary conditions were defined for the sediment. Given that mud-rich WSFM deposits were found over the Atchafalaya inner shelf (Denommee et al. 2016), noncohesive sediment dynamics was simplified as sand was treated as a resuspension-resistant sediment class (τ_{cri}=100 Pa, Equation 1). On the seafloor, four sediment layers were initially prescribed with 1 m thickness for each layer, and their thicknesses evolved with deposition and erosion. The percentage of cohesive sediment on the seafloor was based on the usSEABED data set (Williams et al. 2006). Because the WSFM process has been primarily reported on the topset and foreset of the subaqueous delta (water depth < 10 m; Allison et al. 2000; Denommee et al. 2018; Denommee et al. 2016; Draut et al. 2005), the mud fraction over the seabed was prescribed as zero where water depth exceeded 10 m.

The same computational grid was used in SWAN (Table 2) as in ROMS. Similar to the oceanic model application, wave boundary conditions for the nGoM were derived from the parent GoM model (Zang et al. 2019). The SWAN was initialized from a default flat ocean (no wave) and the first simulation month (i.e., January 2021) was treated as the model spin-up period. The wind forcings were from the NCEP CFSv2 6 hourly products. The computational time step was set to 300 s, which was also the time step for the ROMS and SWAN exchange variable information. The third-generation mode for wind input, quadruplet interactions and whitecapping was implemented with an exponential wave growth scheme and whitecapping scheme by Komen et al. (1984) selected. The depth-induced wave-breaking process was defined with a constant breaker index applied (proportionality coefficient of the rate of dissipation=1.0, the ratio of maximum individual wave height over depth=0.73). Madsen et al.'s (1988; Madsen and Rosengaus 1988) bottom friction scheme was activated with the equivalent roughness length scale of the bottom as 0.05.

The coupled model output daily historical snapshots of multiple hydrodynamic and sediment parameters, including 3-dimensional current velocity components, water temperature, salinity, water level, 2-dimensional current velocity, significant wave height, mean wave direction, peak surface wave period, fluid mud concentration, fluid mud thickness, and sediment bed layer thickness. The probability of fluid mud events (also referred to fluid mud probability), defined as instances where fluid mud concentration exceeds 10 g/L over a specified period, was calculated. Sedimentation rate was determined by the rate of change in total sediment bed layer thickness during a given period. Detailed analysis of these sediment-related parameters is presented in the subsequent results section (Section 4.7).

Table 2 Configurations of coupled ROMS (with CSTMS+WBL)–SWAN model for NGOM application

Model	ROMS (with CSTMS+WBL)	SWAN
Resolution	1 km (horizontal) and 24 sigma layers (vertical)	1 km
Simulation period	January 1, 2021–December 31, 2021, with the January as the spin-up period	January 1, 2021–December 31, 2021, with the January as the spin-up period
Computational time step	1 s	300 s
Open boundary	(1) Free surface height (Chapman implicit scheme forced by GOM-5km hindcast) (2) Depth-integrated current velocity (Flather scheme forced by GoOM-5km hindcast)	Forced by GOM-5km hindcast

Model	ROMS (with CSTMS+WBL)	SWAN
	(3) Three-dimensional current velocity (mixed radiation-nudging scheme forced by GOM-5km hindcast) (4) Water temperature (mixed radiation-nudging scheme forced by GOM-5km hindcast) (5) Water salinity (mixed radiation-nudging scheme forced by GOM-5km hindcast) (6) Cohesive and noncohesive sediment classes (radiation scheme; no prescribed boundary forcing)	
Bottom boundary	(1) Four sediment layers with 1 m thickness for each (2) Percentage of cohesive sediment from the usSEABED database (3) Mud fraction at seabed as zero where depth > 10 m	Not valid
Initial conditions	From GOM-5km hindcast: (1) Free surface height (2) Depth-integrated current velocity (3) Three-dimensional current velocity (4) Water temperature (5) Water salinity	Default flat ocean (no wave)
Atmospheric forcings	CFSv2 6-hourly products: (1) precipitation rate (2) sea surface air pressure (3) net longwave radiation flux (4) net shortwave radiation flux (5) winds at 10 m height (6) air temperature at 2 m height (7) relative humidity at 2 m height	CFSv2 6-hourly winds at 10 m height
River forcings	USGS: (1) 63 source points for Atchafalaya and Mississippi rivers (2) Daily river discharges, temperature, salinity, and fluvial sediment concentration	Not valid
Time steps for information exchanges	ROMS sends current velocity, water level, and dynamic depth to SWAN every 300 s	SWAN sends wave information to ROMS every 300 s
Output	Daily historical snapshots of hydrodynamic and sediment variables	Daily historical snapshots of wave variables
Others	--	(1) Third-generation mode for wind input with an exponential wave growth scheme (2) Quadruplet wave interactions (3) Whitecapping scheme by Komen et al. (1984) (4) Depth-induced wave-breaking process with a constant breaker index applied (5) Bottom friction scheme by Madsen et al. (1988)

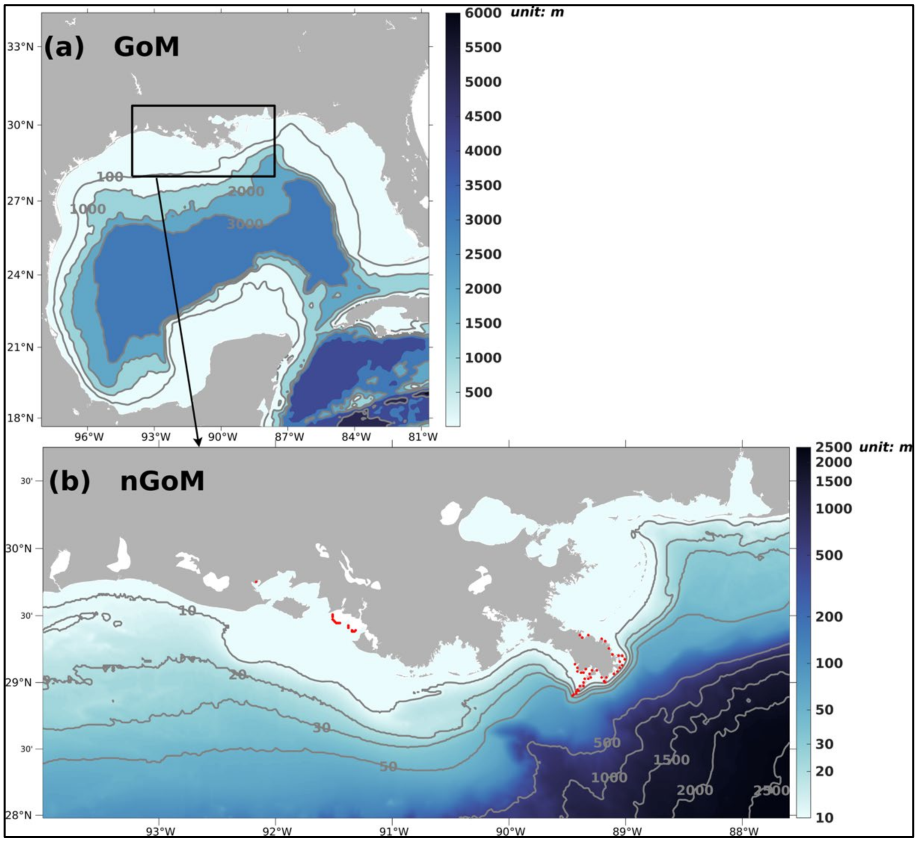

Figure 13. Bathymetry of computational domains.

The top panel (a) is for the parent GOM model and the bottom panel (b) for the child NGOM model. Red dots indicate the locations of river point sources defined in the NGOM model.

4. Results

4.1 Sediment Characteristics

4.1.1 Vibracores

An in-depth analysis of the vibracores from the study reveals distinct density and grain size distributions within the Raccoon Island dredge pit compared to its surroundings (Zhang et al. 2023). Average densities observed within the pit (1.78 g/cc) are notably lower than those outside the pit (1.9 g/cc) (Table 3). This variance indicates a finer sediment texture within the pit, characterized primarily by fine silt, while sediments outside the pit often include coarser silt and occasional very fine sand layers.

Table 3. A summary of density, grain size, organic matter, and carbonate data from vibracores of RI1, 2, 3, 4, 5, and 9

Core#	Density	(g/cc)	Grain size	(phi)	Sand (%)	Organic matter	(%)	Carbonate	(%)	Om/ Carb
--	range	mean	range	mean	mean	range	mean	range	mean	mean
RI1	0.64~1.97	1.62	5.93~6.93	6.44	8.62	5.09~5.58	5.25	1.03~1.50	1.34	3.92
RI2	0.13~2.38	1.72	5.64~6.90	6.30	9.38	3.69~5.21	4.89	1.36~2.63	1.77	2.76
RI3	1.51~2.30	1.91	4.19~6.11	5.59	15.9	3.44~6.56	4.91	1.07~2.00	1.35	3.64
RI4	0.24~2.31	1.86	4.00~7.00	6.02	13.03	4.25~6.86	5.20	1.37~3.36	2.26	2.3
RI5	1.34~2.31	2.04	3.50~8.36	6.25	21.76	1.94~6.85	4.75	1.07~2.77	1.84	2.58
RI9	1.48~2.26	1.76	4.94~7.29	5.95	24.22	1.92~5.69	3.54	0.81~1.98	1.34	2.64

See Figure 12c for locations. Om is organic matter and Carb is carbonate (from Zhang et al., 2023).

Grain size measurements highlight significant textural differences (Figure 15). Inside the pit, sediments exhibit a smaller, more uniform grain size, with a median range of 4.0–7.0 phi (Figure 16), indicating a stable deposition environment. In contrast, sediments from outside the pit show greater variability in grain size (3.50–8.63 phi), suggesting dynamic sedimentary processes driven by external factors like tidal currents and storm events.

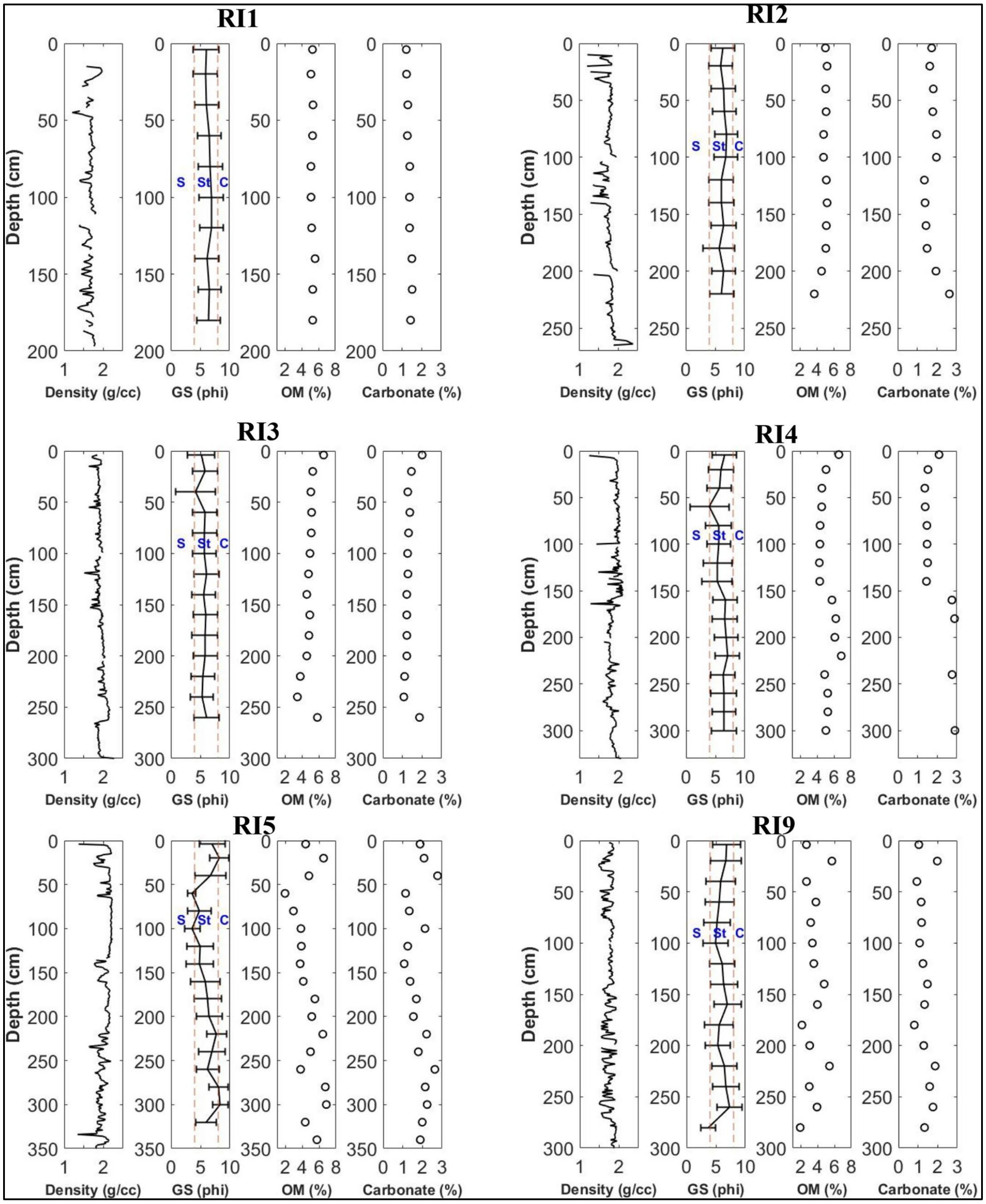

Figure 14. Density, grain size, and standard deviation, organic matter, and carbonate content from Raccoon Island pit and shelf.

RI1, RI2, RI3, and RI4 are sediment cores collected inside the Raccoon Island dredge pit. RI5 and RI9 are cores outside (Figure 12). ‘S’, ‘St’ and ‘C’ are sand, silt and clay, respectively. GS represents grain size, while OM is organic matter (from Zhang et al., 2023).

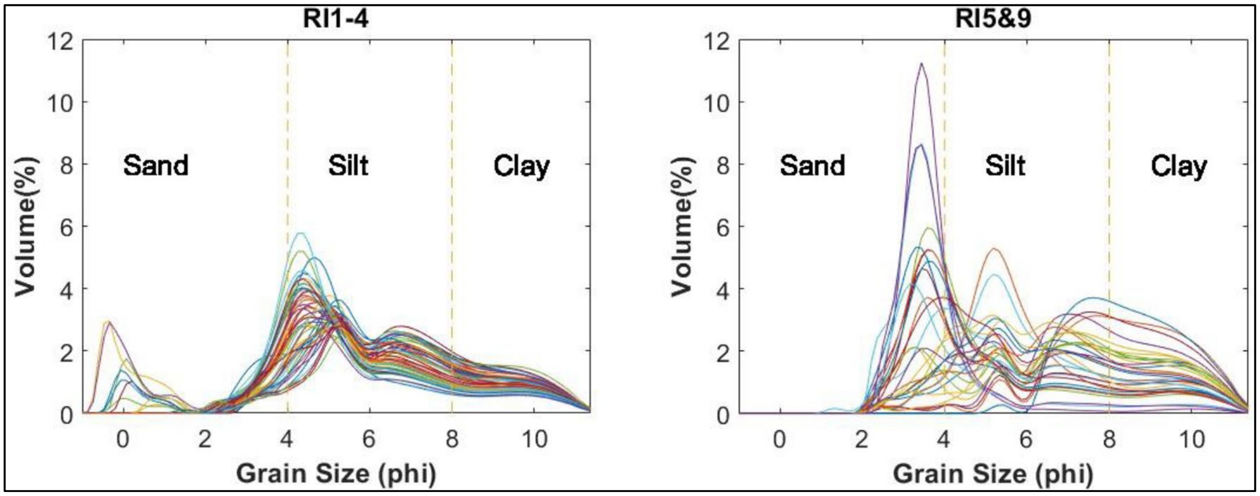

Figure 15. Sediment grain size distribution.

The left panel, RI1–4, represents four cores collected from inside the Raccoon Island dredge pit. The right panel, RI5and RI9, are cores outside the dredge pit (Figure 12). Tan-colored dashed vertical lines are 4 phi and 8 phi (from Zhang et al., 2023; For interpretation of the references to color in this figure legend, the reader is referred to Zhang et al., 2023.)

Organic matter and carbonate content analyses also support these observations, with higher average organic matter (5.06%) and carbonate (1.68%) contents found inside the pit compared to outside (Table 2). This suggests that the depositional environment within the pit may support different biological activities, likely due to its more stable and finer sediment matrix, which can host a distinct community of benthic organisms compared to more turbulent external areas. The dredge pit is an organic and carbonate “sink”. The variability outside the pit was greater than inside the pit for organic matter (Figure 15). It is highly possible that the rapid infilling in pit as opposed to long-term record of the outside pit cores.

4.1.2 Multicores

Grain size analysis of multicore samples shows that seabed surface of infilling Raccoon Island dredge pit and nearby stations is dominated by coarse silt, ranging from 3.8 to 5.3 phi (Table 4; Figure 18). At Station C, fine sandy layers are found between 4 and 10 cm, with grain sizes from 2 to 3.7 phi (Figure 17 and Figure 18). From March 2020 to March 2021, grain size remained relatively stable at Stations B and D, while Stations A and C exhibited significant variations (Figure 17).

LOI data from multicore samples indicate that organic matter percentages range from 1.22% to 9.98%. Station B has the highest mean organic matter at approximately 8.27%, while station C has the lowest mean organic matter of 2.09% (Table 4). Carbonate content (mainly shell fragments) ranges from 0.63% to 9.94%. Station B recorded the highest mean carbonate in March 2022, reaching 3.1%. Conversely, Station C had the lowest carbonate percentage in March 2021, at 1.05%. The most significant differences in organic matter and carbonate content were observed at Stations B and C (Figure 19). Additionally, two carbonate-rich layers were identified at Station D in summer 2021 and spring 2022 (Figure 19).

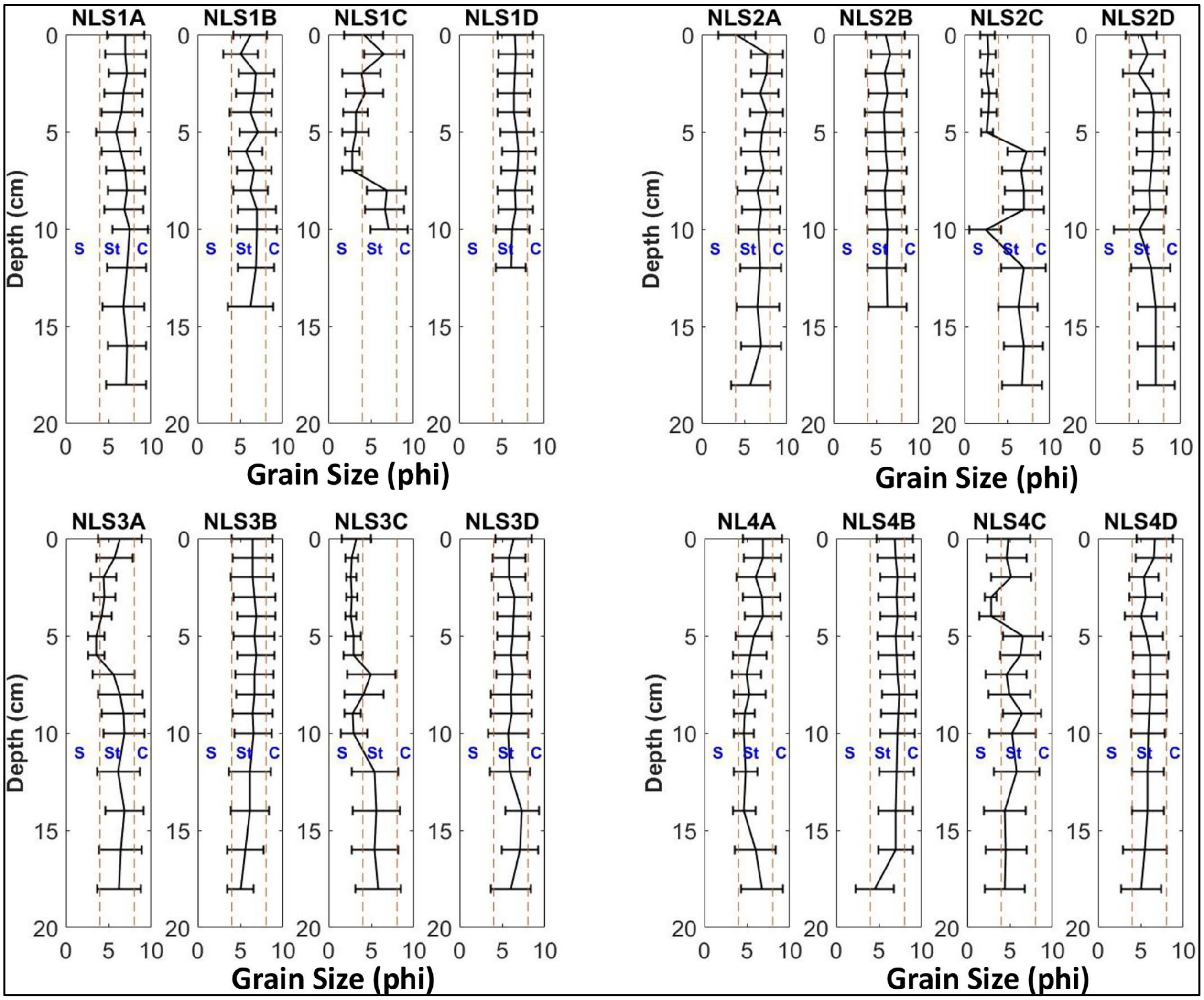

Figure 16. Multicore median grain size data from cruises 1, 2, 3, and 4.

Multicores from four stations were collected during each cruise. Station B is inside the pit and station C is south of the pit and closer to Ship Shoal. Tan-colored dashed lines mark the range of silt (Figure 12). 'S', 'St' and 'C' are sand, silt and clay, respectively (from Zhang et al., 2023; For interpretation of the references to color in this figure legend, the reader is referred to Zhang et al., 2023).

Table 4. A summary of grain size, organic matter, and carbonate data from multicores

Core#	Grain size	(phi)	Sand (%)	Organic matter	(%)	Carbonate	(%)	Om/Carb
--	range	mean	mean	range	mean	range	mean	mean
NLS1A	5.80~7.52	6.89	9.87	3.82~6.67	5.22	0.81~3.73	1.94	2.69
NLS1B	5.07~7.09	6.43	11.6	3.33~7.89	4.31	0.87~3.74	1.77	2.44
NLS1C	2.84~7.08	4.45	52.88	2.07~4.55	2.73	0.65~1.66	1.05	2.6
NLS1D	6.07~7.00	6.57	4.66	3.91~8.75	6.08	1.36~2.50	1.95	3.12
NLS2A	4.14~7.66	6.77	12.27	3.28~5.71	4.28	1.32~9.94	2.40	1.78
NLS2B	5.88~6.62	6.18	11.4	5.51~9.48	7.19	1.59~2.67	2.03	3.54
NLS2C	2.45~6.93	4.91	46.22	1.39~4.92	2.52	0.66~4.73	1.49	1.69
NLS2D	5.01~7.13	6.38	9.23	1.90~6.22	4.54	1.54~7.98	2.50	1.82
NLS3A	3.52~6.86	5.55	23.6	1.84~7.89	4.15	1.98~5.79	2.95	1.41
NLS3B	5.01~6.81	6.36	13.69	2.43~8.49	6.87	1.18~3.69	2.66	2.58
NLS3C	2.63~5.77	3.79	67.9	1.30~3.40	2.09	0.63~1.94	1.07	1.95
NLS3D	5.66~7.33	6.22	10.95	2.59~6.41	4.52	1.87~3.28	2.48	1.82
NLS4A	4.67~6.84	5.75	12.83	1.58~8.11	4.33	1.08~3.13	1.97	2.2
NLS4B	4.53~7.35	6.92	7.59	5.71~9.98	8.27	2.00~4.14	3.10	2.67
NLS4C	2.78~6.58	4.90	44	1.22~3.12	2.40	0.78~1.73	1.21	1.98
NLS4D	5.02~6.62	5.82	12.98	2.42~5.72	4.10	1.28~4.04	2.44	1.68

Om is organic matter and Carb' is carbonate (from Zhang et al., 2023).

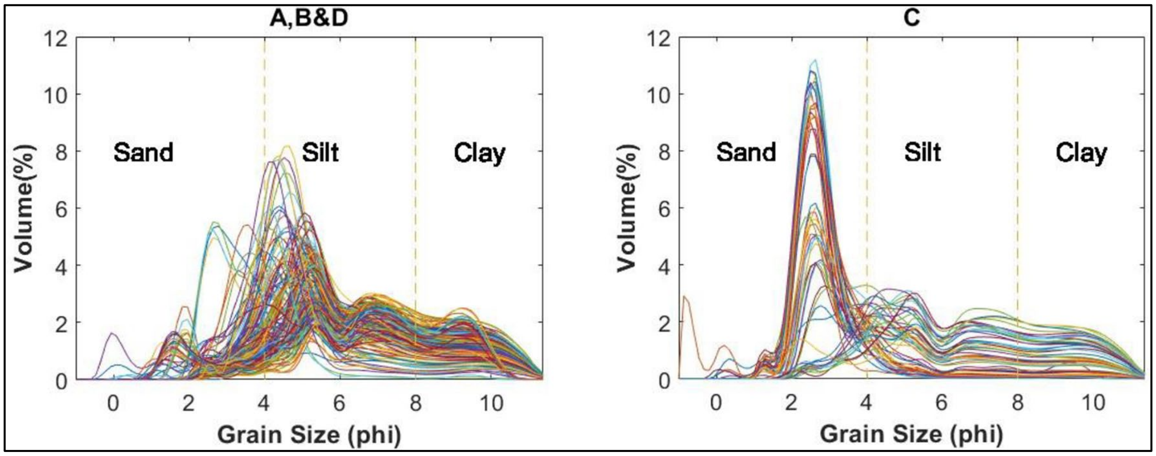

Figure 17. Multicore sediment grain size distribution.

The left panel represents all multicores collected from station A, B, and D; the right panel represents all multicores from station C. Tan-colored dashed vertical lines are 4 phi and 8 phi. (from Zhang et al., 2023; For interpretation of the references to color in this figure legend, the reader is referred to Zhang et al., 2023).

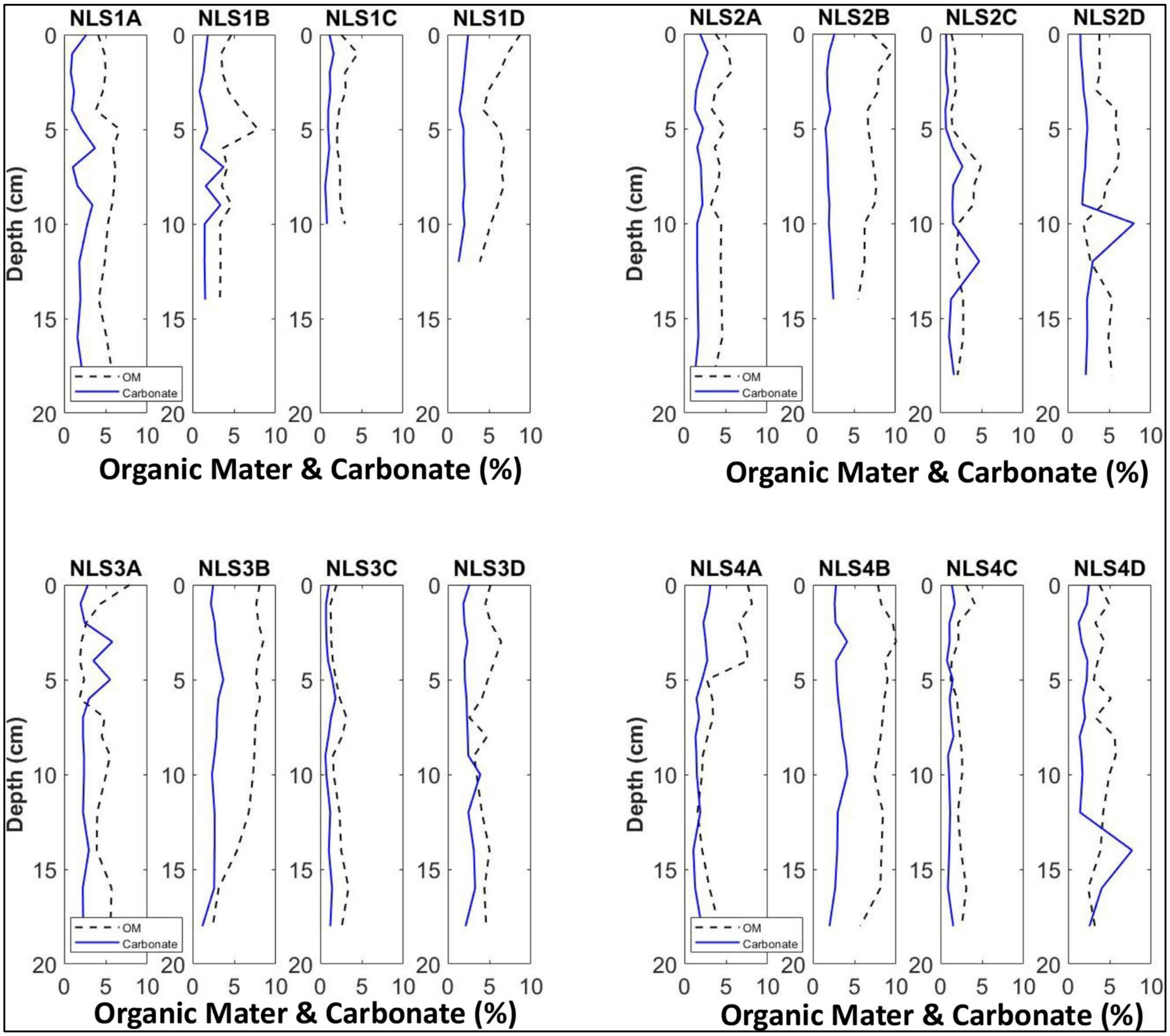

Figure 18. Organic matter and carbonate data from multicores collected from stations A, B, C, and D.

Black dashed lines represent organic matter; blue solid lines represent carbonate (Figure 12) (from Zhang et al., 2023). For interpretation of the references to color in this figure legend, see Zhang et al., 2023).

4.2 Radionuclide Analysis (^{7}Be)

In March 2021,^{7}Be penetration was deepest at Station B (dredge pit) down to 6 cm (Figure 20). Station C had ^{7}Be penetration down to 4 cm, with Stations D and A having the shallowest ^{7}Be penetration at 2 and 1 cm, respectively. This would be roughly the same pattern throughout every sampling, with Station B having the deepest ^{7}Be penetration during each sampling, Station C with the second deepest, and Station A and D alternating as the shallowest stations with the least ^{7}Be penetration. Station B was the only one to have ^{7}Be presence throughout the entire core of 20 cm for one sampling (March 2022), with July 2021 and November 2021 being close, with 16 cm of ^{7}Be presence detected. At no other station or sampling period was ^{7}Be detected deeper than 10 cm, with only Station C during March 2022 having ^{7}Be detection at a depth of 10 cm.

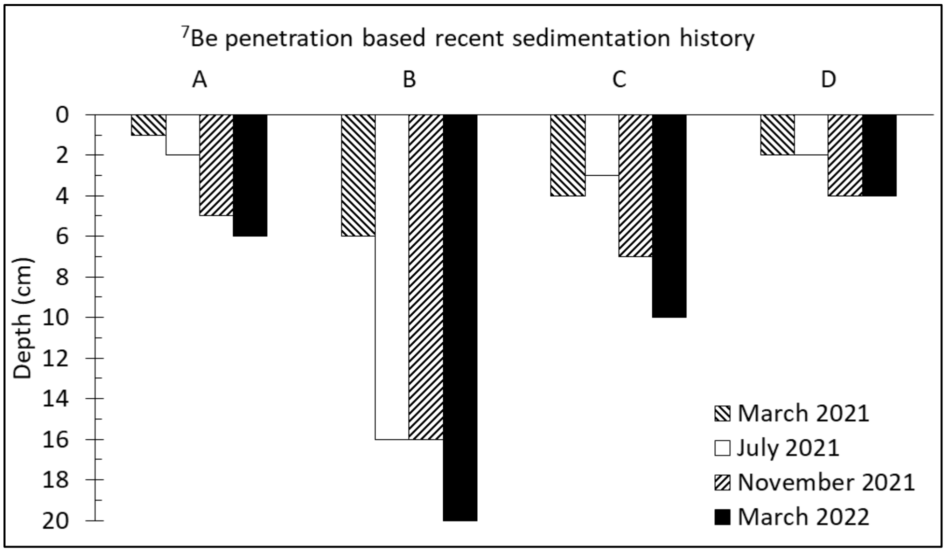

Figure 19. Beryllium-7 sediment penetration spatially and temporally.

4.3 Incubation Chemistry

Sediment oxygen consumption (SOC) rates were calculated from a triplicate of sediment cores collected using multicores. The rates are calculated for each individual core by assuming a linear drop in O_2 concentration over time and reported as an average of the three cores with an uncertainty equal to its standard deviation. The SOC rates seemed to follow clear seasonal patterns. The greatest SOC rates across all stations were during July 2021 (Figure 21), with Stations A, B, C, and D having SOC rates of 26.43 ± 6.09 mmol m^{-2} d^{-1}, 36.05 ± 6.49 mmol m^{-2} d^{-1}, 42.25 ± 1.26 mmol m^{-2} d^{-1}, and 40.77 ± 4.54 mmol m^{-2} d^{-1} respectively. The water temperature for the incubation during July 2021 was 28°C, while all other incubations were set to 20°C, thereby indicating summer temperatures as a major factor behind the higher SOC rates. The SOC for the rest of the time across stations was relatively the same, with all the remaining SOC values having an average of between 5 and 13.5 mmol m^{-2} d^{-1}. These SOC values are far off the values of July, thus indicating a difference in SOC rates between seasons across all stations.

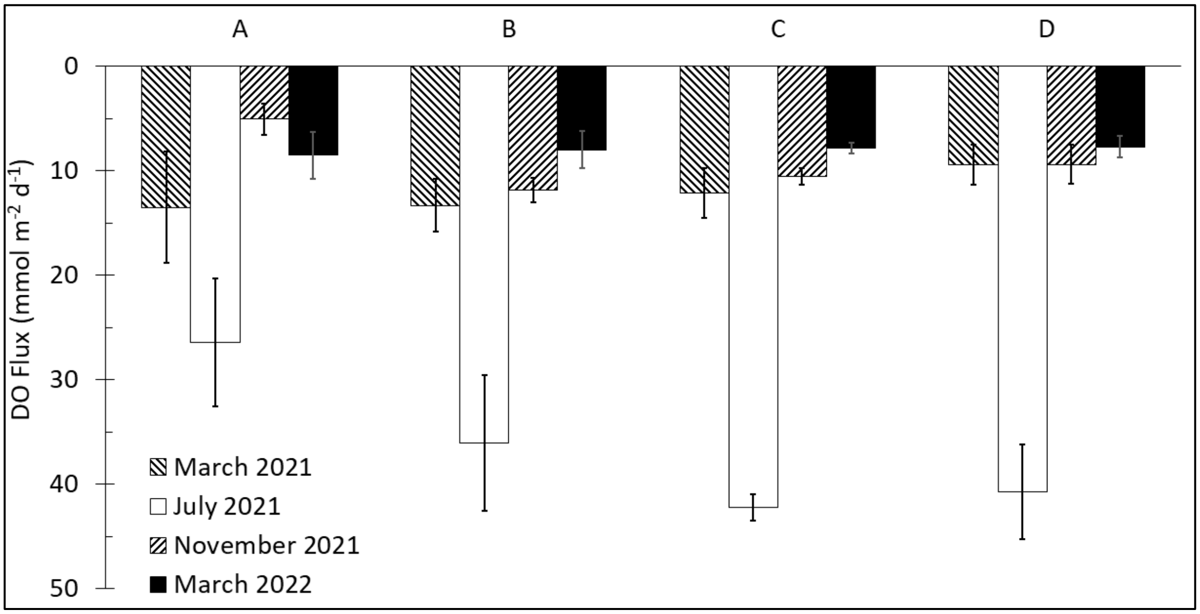

Figure 20. Seasonal DO flux across all stations.

July had an incubation temperature of 28°C and all other times having an incubation temperature of 20°C.

4.4 Total Organic Carbon and Total Nitrogen

Organic carbon content did not show much variability with depth. The total organic carbon (TOC) content from the top 6 cm is averaged and presented in Figure 22. Station B had the highest percentage of organic carbon among all stations, with 1.79% in July 2021, 1.59% in November 2021, and 1.77% in March 2022. In March 2021, Station B did not have the highest TOC content, with a TOC content of 0.94%, compared with Station D, which had a TOC content of 1.02% but the difference was not statistically significant. C had the lowest organic carbon percentage across the entire time of the study, ranging between 0.19% and 0.57% (Figure 22).

The same general pattern was observed for total nitrogen (TN) as well. B had the highest percentage in July 2021 (0.13%), November 2021 (0.17%) and March 2022 (0.17%) (Figure 22). Again, only D had a slightly higher total nitrogen percentage during March 2021 (0.1%) compared with B (0.09%). C had the lowest total nitrogen percentage throughout the study, ranging from 0.03% to 0.06%).

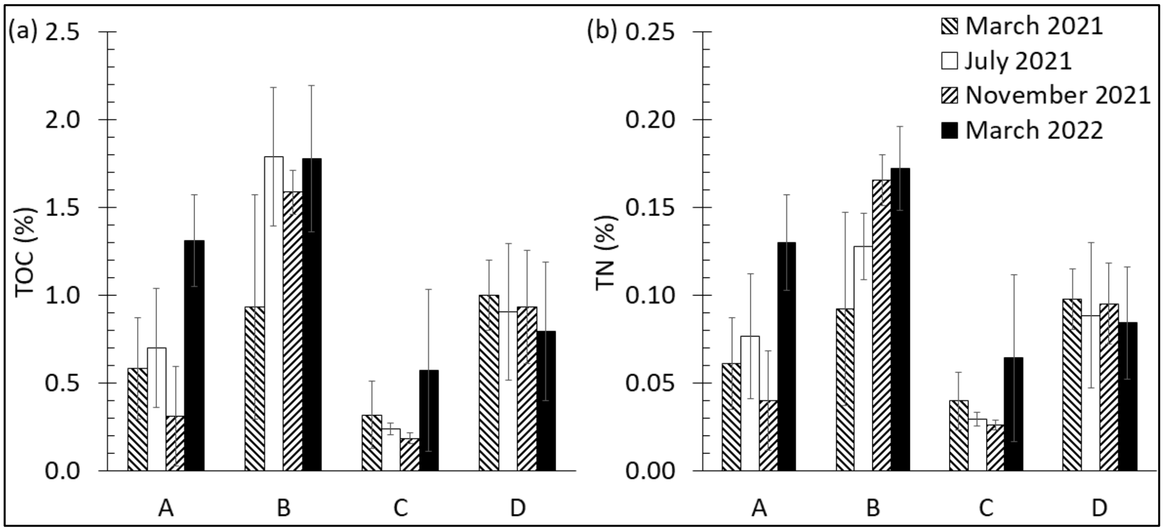

Figure 21. Left panel (a) seasonal change of total organic carbon (TOC%) and right panel (b) total nitrogen (TN%) in sediment across all stations from the top 6 cm (Figure 12).

4.5 Geophysical Data

4.5.1 Sidescan Sonar

A side-scan mosaic map in the 2015 survey showed dark zones inside the pit with low backscatter values where bathymetry indicated the depth was deeper when compared to outside the pit (Figure 23 left). This dredge pit seems to be an effective sediment trap in 2015. The dark zone inside the pit becomes lighter and extends to the west and south sides of the pit in the side-scan mosaic 2018 (Figure 23 middle). This enlarged brown area could be the infilling sediment's redistribution. Its extension to the west and north also indicates the west side of the pit wall is in the dominant current direction. Regardless of the difference of the data collecting frequency of these three datasets, a depth difference within and without the dredge pit occurred in the sidescan data in 2021 (Figure 22). Combined with the evidence from the bathymetry data (not shown in this report; Zhang et al., in prep), a new subsidence can also be confirmed from by the sidescan data. One low reflectivity area is found on the east side of the dredge pit (Figure 23 right). The east side of the dredge pit and the east side of the dark area look parallel to each other. There is no evidence to show that the shaded area parallel to the dredged area was noise.

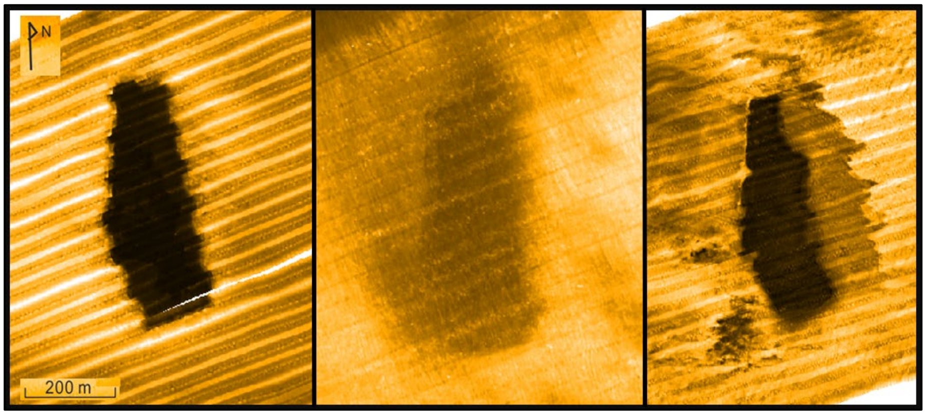

Figure 22. Side-scan mosaic maps of Raccoon Island pit for three post-dredging surveys on 06/2015 (left), 08/2018 (middle), and 10/2021 (right).

Brighter colors indicate high backscatter, while darker colors indicate lower backscatter. (Data from 2015 and 2018 are from Liu et al., [2020]).

4.5.2 CHIRP Seismic Profiles

Subbottom chirp seismic profiles collected in the Raccoon Island dredge pit in 2015, 2018, and 2021 reveal multiple layers in stratigraphy (Figure 24). The most prominent features are the remnants of the buried paleo river channel in the surrounding area outside of the dredge pit. Within the pit area, there is a wide acoustically-opaque infill inside the pit. A half meter subsidence occurred in the chirp seismic profiles from 2021 (Figure 24). This is the first time that a subsidence occurred on an infilled dredge pit. Bigenic gas (darker layer) was found in the infilling sediment layer inside the pit and degassing (bubbling, e.g., above red dashed line in panel D in 2021) was found in the water column above the pit (Figure 24).

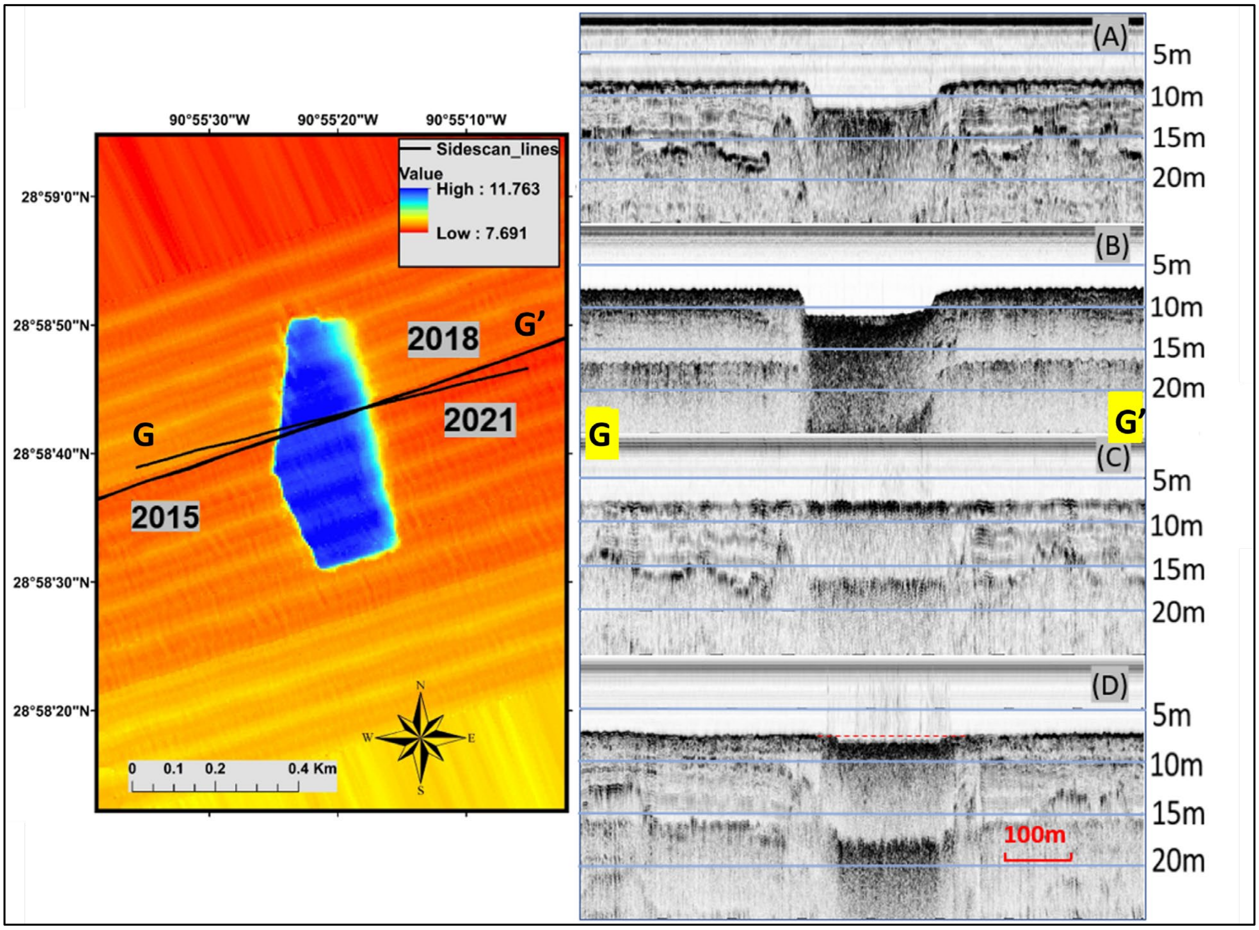

Figure 23 Sub-bottom seismic profiles collected across Raccoon Island dredge pit in 2015, 2018, and 2021.

Top right panel (A) and top-mid right panel (B) come from chirp seismic profiles 2015 but different frequency (A) and (B) from Edgetech 512i and 2000 DSS, respectively). Mid-center right panel (C) and lower right panel (D) come from chirp seismic profiles 2018 and 2021 respectively. The track lines on each bathymetry map are the location of Chirp seismic profiles. G and G mark the orientation of subbottom track lines. The blue area on the map is the Raccoon Island dredge pit. Bathymetry data used in this map was collected in 2015.

4.6 Benthic Ecology

4.6.1 Macrofauna

There was no main effect difference among sites (Table 5). There was a difference between seasons and site by season interaction (Table 4). An interaction between site and season indicates that results at sites were not consistent across seasons.

Table 5. PERMANOVA model results for benthic macrofauna collected at four sites in and around the Raccoon Island dredge pit in spring, summer, and fall 2021 and summer 2022

--	Df	SumSqs	R2	F	Pr(>F)
Site	3	0.56	0.06	1.19	0.22
Season	3	1.45	0.14	3.07	0.001
Site:Season	9	2.80	0.28	1.98	0.001
Residual	34	4.20	0.53		

Df = degrees of freedom, SumSqs = Sum of Squares, R2 = the percentage of variation in the response that is explained by the model, F = F statistic, Pr(>F) = p value.

Since there was an interaction effect between site and season, seasonal effects must be interpreted for each site individually. Since benthic community composition data is multivariate, graphical methods of viewing the data must summarize multi-dimensional species abundance data in a few dimensions to ease interpretation. A common way to do this in the field of community ecology is to use a Principal Component Analysis.

A Principal Component Analysis is a visualization tool used to represent data in a lower-dimensional space while preserving as much of the key information as possible, making it easier to explore patterns in the data. The PCA algorithm identifies new variables called principal components (PCs), which are linear combinations of the original variables. The first principal component (PC1) captures the direction of the greatest variance in the data. The second principal component (PC2) is orthogonal to PC1 and captures the next highest variance, and so on. The axes of the PCA plot represent the principal components. Typically, PC1 is on the x-axis, and PC2 is on the y-axis. Each point on the plot corresponds to a data sample (e.g., an observation or an individual) from the original dataset, now represented in the lower-dimensional space.

Data points that are close to each other in the PCA plot are similar in the original high-dimensional space, while points that are far apart are more dissimilar. Clustering in a PCA plot might reveal groups, patterns, or trends in the data that were not easily identifiable in the original, multidimensional species abundance matrix. In the following PCA plots, you'll also see vectors or arrows. These represent the correlation between the abundance of an individual species and the PCs. For example, in (Figure 25), the vector labeled *Nassarius acutus* (a type of snail) is aligned well with PC1. Samples from Spring 2022 separate out from the rest along PC1, in the direction of the *N. acutus* vector. This indicates that one major reason these samples were different from the rest is relatively high abundance of *N. acutus* (Figure 25).

Site A was one cause of the site by season interaction. The community at Site A was altered during spring 2022. This can be seen in Figure 25. The species present were primarily sand-dwelling and scavenging snails *Nassarius acutus* and other sand-dwelling species (Figure 25). There were relatively few deposit-feeding, early colonizing polychaetes such as *Magelona* spp. This pattern is indicative of a recent sand deposition event with low organic matter.

Site B was also a cause of the site by season interaction. In spring 2021 and summer 2021, very few organisms were found at Site B. The community was altered during fall 2021 and spring 2022. In fall 2021, *Capitella capitata* and *Sigambra tentaculata*, opportunistic polychaetes that do well with lots of organic matter, colonized site B (Figure 26). By spring 2022, the composition had changed again. The species gained were filter- and deposit-feeding bivalves *Mulinia lateralis* and *Tellina versicolor* (Figure 26). These community composition changes are indicative of burial and/or disturbance and early recovery.

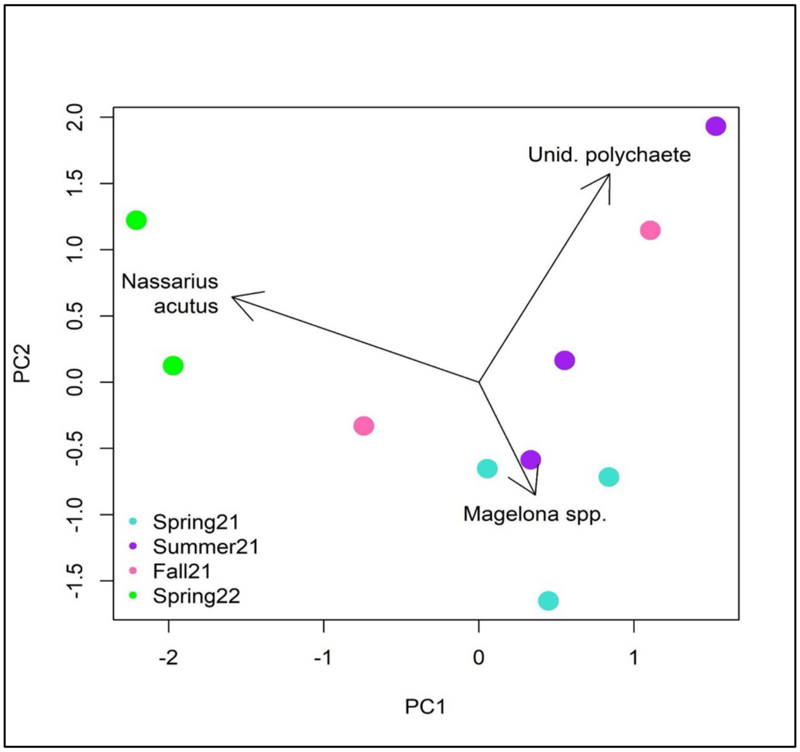

Figure 24. PCA plot for Bray-Curtis dissimilarity matrices of square-root transformed macrofaunal community composition data for site A.

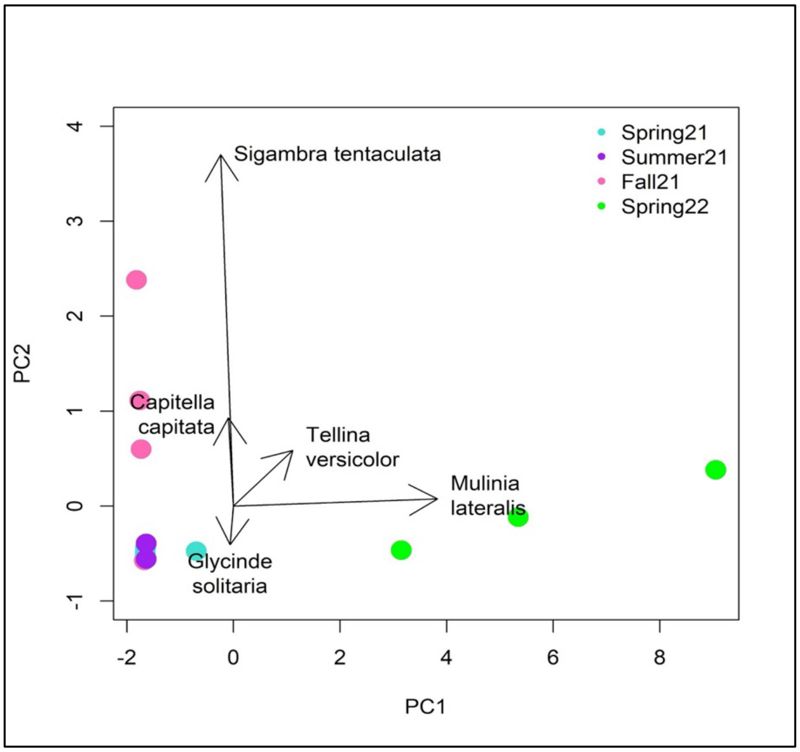

Figure 25. PCA plot for Bray-Curtis dissimilarity matrices of square-root transformed macrofaunal community composition data for site B.

4.6.2 Meiofauna

There was a difference among sites, a difference among seasons, and a site by season interaction (Table 6).

Table 6. PERMANOVA model results for benthic meiofauna collected at four sites in and around Raccoon Island dredge pit, in summer and fall 2021, and in summer 2022

--	Df	SumSqs	R2	F	Pr(>F)
Site	3	0.96	0.12	1.75	0.02
Season	2	1.28	0.16	3.52	0.001
Site:Season	6	1.55	0.20	1.42	0.04
Residual	22	4.00	0.51		

Df = degrees of freedom, SumSqs = Sum of Squares, R2 = the percentage of variation in the response that is explained by the model, F = F statistic, Pr(>F) = p value.

Spring 2022 was the cause of the site by season interaction. The community composition differed among sites in spring 2022 only. Many opportunistic *C. capitata* recruited to site C in the spring (Figure 27). At site B, new recruits were primarily the deposit-feeding bivalve *Tellina versicolor* (Figure 27).

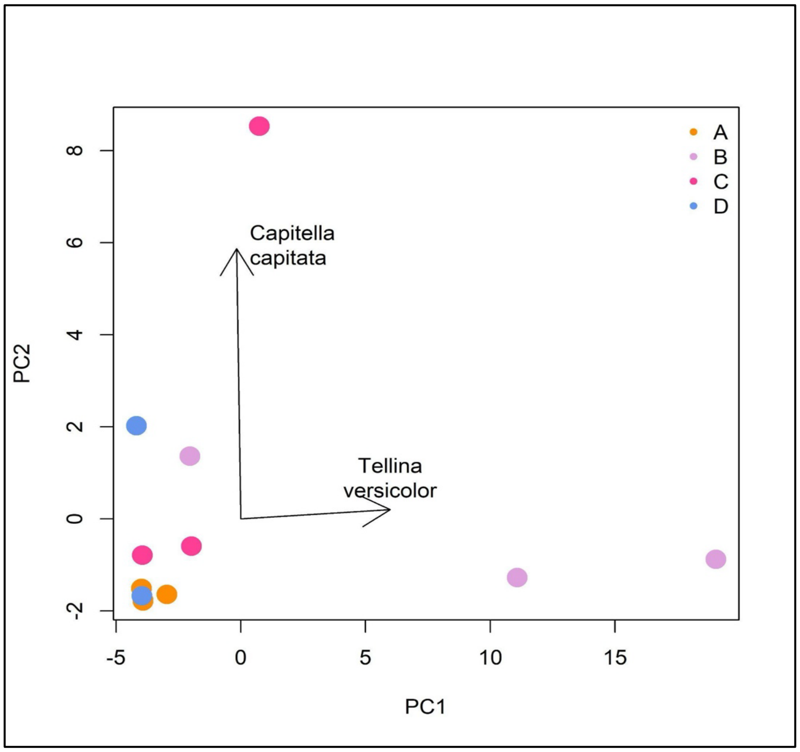

Figure 26. PCA plot for Bray-Curtis dissimilarity matrices of square-root transformed meiofaunal community composition data for spring 2022.

4.6.3 Legacy Data

Species diversity of shelf macrofauna samples from 2013 was generally low with a Shannon diversity index less than 1.5 for nearly all samples. There was no clear relationship between species diversity and the spatial distribution of fluid mud layer thickness (Figure 28). The few samples from an area of high hypoxia frequency tended to have lower diversity than sampled with lower hypoxia frequency (Figure 28).

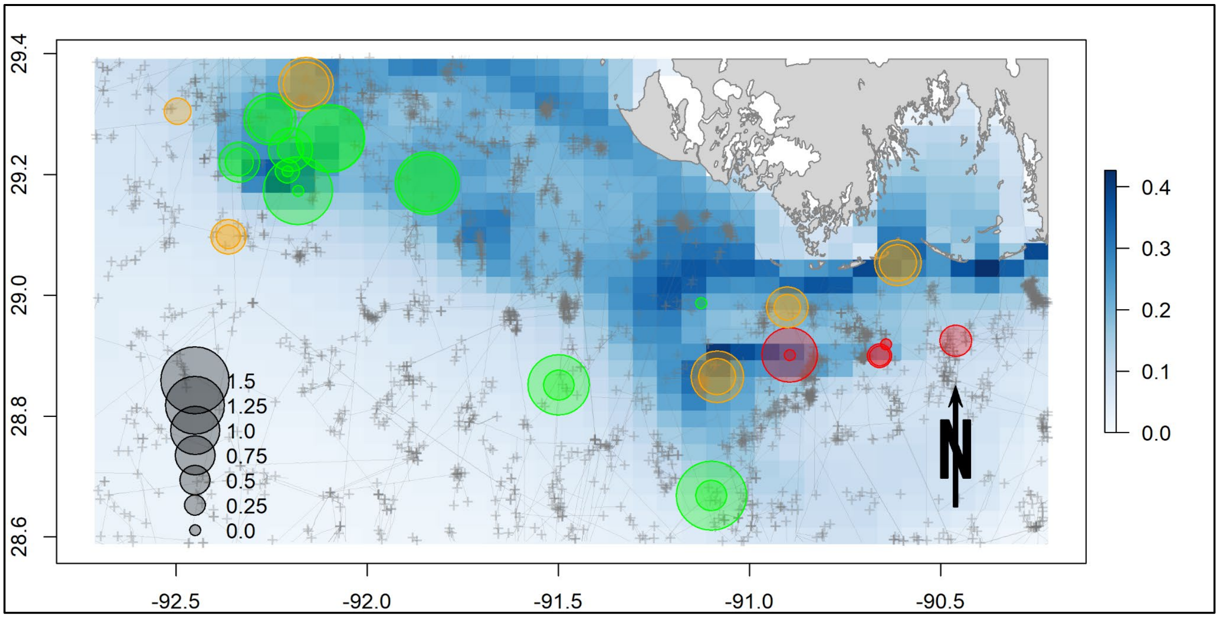

Figure 27. Shannon diversity of macrofauna samples from 2013 on the Louisiana shelf.

Larger circles represent higher species diversity of benthic macrofauna. Annual mean fluid mud thickness (mean_fm) in m as a gradient with deeper blue indicating a thicker fluid mud layer. The frequency of bottom hypoxia from the annual hypoxia cruise 1985-2014 is indicated by a circle color, with high risk equal to hypoxia frequency of 75% or greater (red), moderate risk equal to hypoxia frequency of 50–75% (orange), and low risk equal to hypoxia frequency below 50% (green). Oil infrastructure is represented by thin grey lines (pipelines) and + symbols (oil platforms).

Multiple interactions in the PERMANOVA made the model difficult to interpret the effect of bottom salinity, bottom temperature, bottom dissolved oxygen, and hypoxia frequency. However, mean fluid mud thickness had a significant main effect, and this variable did not appear in any significant interaction effects, which means it is a significant variable driving macroinfauna community composition in the legacy samples (Table 7).

Table 7. PERMANOVA model results for benthic macrofauna collected on the Louisiana shelf in 2013.

The significant main effect was for the annual average fluid mud layer (mean_fm)

--	Df	SumOfSqs	R2	F	Pr(>F)
bottom_salinity	1	0.55	0.04	2.85	0.002
bottom_temp	1	0.11	0.01	0.58	0.83
bottom_DO_mg_L	1	0.14	0.01	0.71	0.73
mean_fm	1	0.5	0.04	2.58	0.01
hypoxia_freq	2	0.52	0.04	1.36	0.14
bottom_salinity:bottom_temp	1	0.52	0.04	2.71	0.01
bottom_salinity:bottom_DO_mg_L	1	0.15	0.01	0.77	0.67
bottom_temp:bottom_DO_mg_L	1	0.53	0.04	2.74	0.002
bottom_salinity:mean_fm	1	0.11	0.01	0.55	0.86
bottom_temp:mean_fm	1	0.32	0.02	1.68	0.08
bottom_DO_mg_L:mean_fm	1	0.27	0.02	1.42	0.18
bottom_salinity:hypoxia_freq	2	0.63	0.05	1.63	0.03
bottom_temp:hypoxia_freq	2	0.45	0.03	1.17	0.27
bottom_DO_mg_L:hypoxia_freq	2	0.42	0.03	1.1	0.33
mean_fm:hypoxia_freq	2	0.53	0.04	1.37	0.14
Residual	24	4.61	0.35		
Total	55	13.06	1		

Df = degrees of freedom, SumSqs = Sum of Squares, R2 = the percentage of variation in the response that is explained by the model, F = F statistic, Pr(>F) = p value.

Model results were interpreted using PCA, as described in section 4.6.1. In the following PCA plot, you'll also see vectors or arrows. The black vector represents the correlation between the abundance of an individual species and the PCs (Figure 29). The blue vectors represent the correlation among the explanatory variables in the model and the PCs (Figure 29).

Amphioxus spp. was responsible for most of the community composition changes among sites, and most of the samples with many *Amphioxus* spp. also had high mean fluid mud layer thickness, evidenced by the close alignment of PC1 and the vector representing *Amphioxus*, and the weak alignment of PC1 and the vector representing mean_fm (Figure 29). *Amphioxus* spp. is a primitive fish-like chordate that is capable of movement in the sediment and water column. It is a selective filter feeder that "coughs" to clear its mouth and branchial filter of unwanted particles.

Amphioxus spp. were not found in sites with average fluid mud layer thickness below 0.2 m. The greatest number of *Amphioxus* spp. found in a single core was in an area with modeled average fluid mud thickness of 0.33 m (Figure 30).

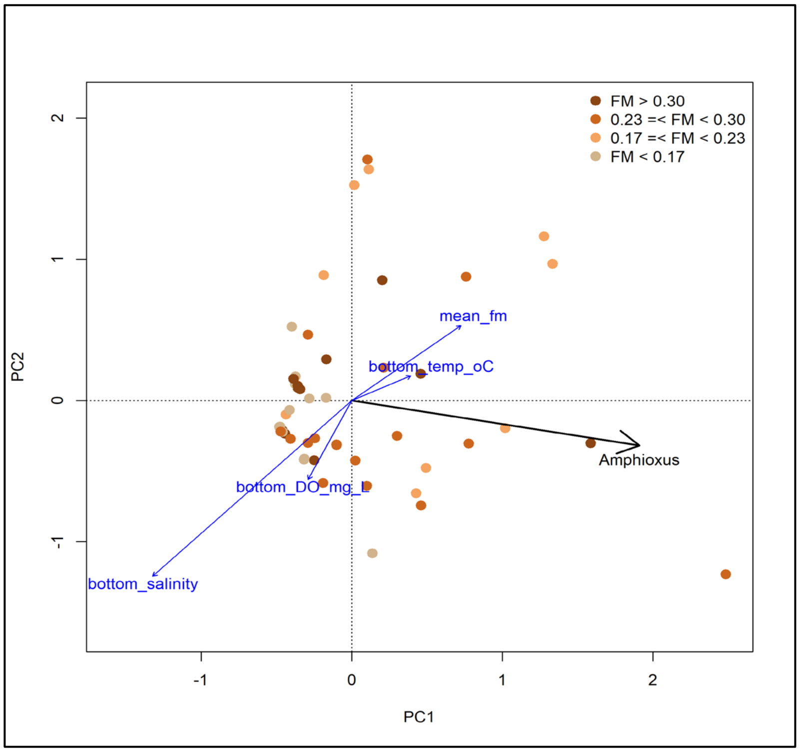

Figure 28. PCA plot for Bray-Curtis dissimilarity matrices of square-root transformed macrofaunal community composition data for 2013.

Points are colored based on modeled fluid mud (FM) layer thickness from the Xue lab, with darker brown indicating a thicker annual average fluid mud layer (mean_fm). Blue vectors indicate the correlation of environmental variables with the PCA axes. The black vector indicates alignment of Amphioxus spp. with the PCA axes.

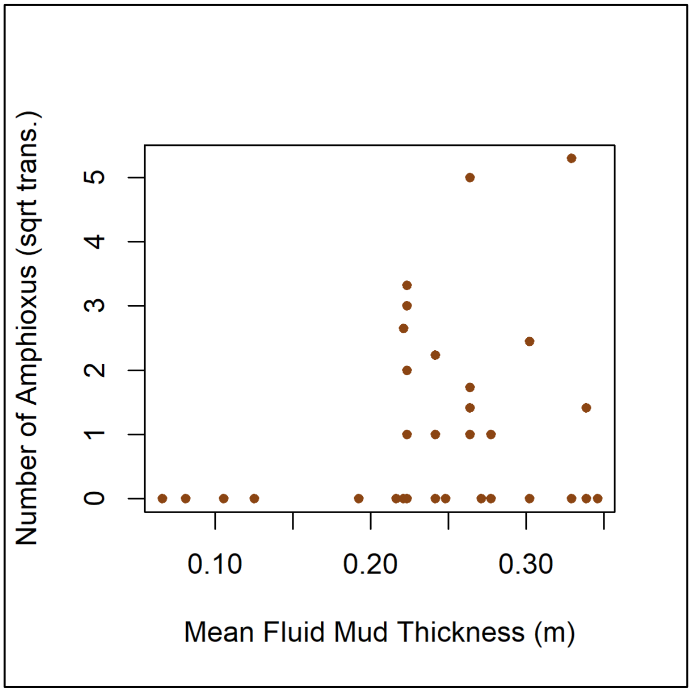

Figure 29. The relationship between mean fluid mud thickness and square-root transformed Amphioxus spp. abundance.

4.7 Fluid-Mud Model

4.7.1 Sedimentation Rate

The sedimentation rate can be estimated by the maximum penetration depth of ^{7}Be, which has a half-life of 53.3 days. A fair assumption for this estimation is that no ^{7}Be deposition is detected in the sediment beyond two half-lives (i.e., 106.6 days) due to the precision of instruments. Given the sample maximum penetration depth of ^{7}Be (Figure 20), the sedimentation rates at the four sample sites are calculated according to Equation 4 and are listed in Table 7. It was found that sedimentation rates at all sites were positive, indicating a net deposition of sediments over the two listed periods (i.e., April–July and August–November 2021). Most rates are in a magnitude of 10^{-2} cm/day except that at site B, reaching 10^{-1} cm/day. Site B, located inside the dredging pit, experienced a more pronounced infilling process during the year 2021 than the site outside the pit (i.e., site C). The model can roughly capture this difference showing that the model sedimentation rate at site B is close to that at site C during the April–July 2021 period, while the rate at site B is one order of magnitude higher than that at site C during the August–November 2021 episode (Table 8). During the April–June 2021 period, modeled results fit well with the ^{7}Be estimates at sites A and C, underestimate the rate at site B, and demonstrate net erosion at site D. These model-measurement discrepancies can also be found for the August–November 2021 period, but biases are found larger at sites A and C (one order of magnitude less than the ^{7}Be-estimated sedimentation rates).

While the model can capture the general net-deposition pattern, model biases occur (Figure 31). The misfits at site B were attributed to the coarse resolution of the model (1 km) compared to the size of the dredging pit (approximately 200×500 m; Figure 12c) and the unrealistic modeled bathymetry inside the pit. The opposite sedimentation patterns based on the model results and ^{7}Be estimates at site D may be introduced by the coarse model resolution and the interpolation method. The modeled rates at sampled sites are interpolated according to the nearest points from the 2-D spatial fields, where site D is located at the edges of the positive and the negative regimes (Figure 31). The squared boundaries between these regimes, resulting from interpolation during contour map generation, may render the sedimentation rates at these boundaries unreliable. In other words, the modeled sedimentation rate at site D could potentially be positive with a finer computational grid. Therefore, the model is thought to be capable of capturing the general net deposition pattern shown by the ^{7}Be penetration rates. It is noted that the ^{7}Be-estimated sedimentation rates cannot fully represent reality as such estimates hardly denote the net erosion pattern. In addition, any unknown and unquantifiable features during the coring operations can affect the measured ^{7}Be penetration depth, most of which is around a few centimeters, and further the ^{7}Be-estimated sedimentation rates. Thus, the coupled model is used for capturing the general sediment dynamics around the Mississippi-Atchafalaya River plume area rather than the precise sedimentation rates at some specific sites.

$$Sedimentation\ rate_{^{7}Be} = \frac{penetration\ depth_{^{7}Be}}{106.6\ days} \quad (4)$$

As a long-term monitoring study, it is critical to understand the sedimentation rates over a long period of time instead of focusing on the differences between two specific dates (Figure 31). The slope of the temporal variations in sediment thickness is obtained for each computational cell from February to December 2021 based on the model's daily output. A general long-term deposition pattern is detected (Figure 32) around the sampled sites with a few net-erosion patches. There are two high deposition regions located near the 8-m and 10-m isobaths south of sampled sites (dark red rectangles in Figure 32). It suggests that sustainable dredging behaviors may be guaranteed over these regions, given possible high sediment infilling rates over a year. As indicated by the ^{7}Be results, the sedimentation rate inside a dredged pit can be one order of magnitude greater than that outside the pit (Table 7). Given this approximation, if a 4-m thickness of sediment is dredged from the high deposition area near the 10-meter isobath, where the background sedimentation rate is approximately 0.1 cm per day, it is possible that the dredged pit will revert to its pre-dredging conditions within a year. It is expected that the dredged area can return to its normal condition quickly, thereby minimizing the impact of dredging activities on the coastal biogeochemical conditions and ecosystem.

Table 8. Sedimentation rates at four sample sites estimated by the maximum penetration depth of 7Be and by the coupled model (in parentheses)

Site	A	B	C	D
April–July 2021	0.0188 (0.0160)	0.1501 (0.0183)	0.0281(0.0228)	0.0188 (-0.0838)
August–November 2021	0.0469 (0.0057)	0.1501 (0.0161)	0.0657 (0.0074)	0.0375 (-0.0532)

Note that the unit of the rate is cm/day.

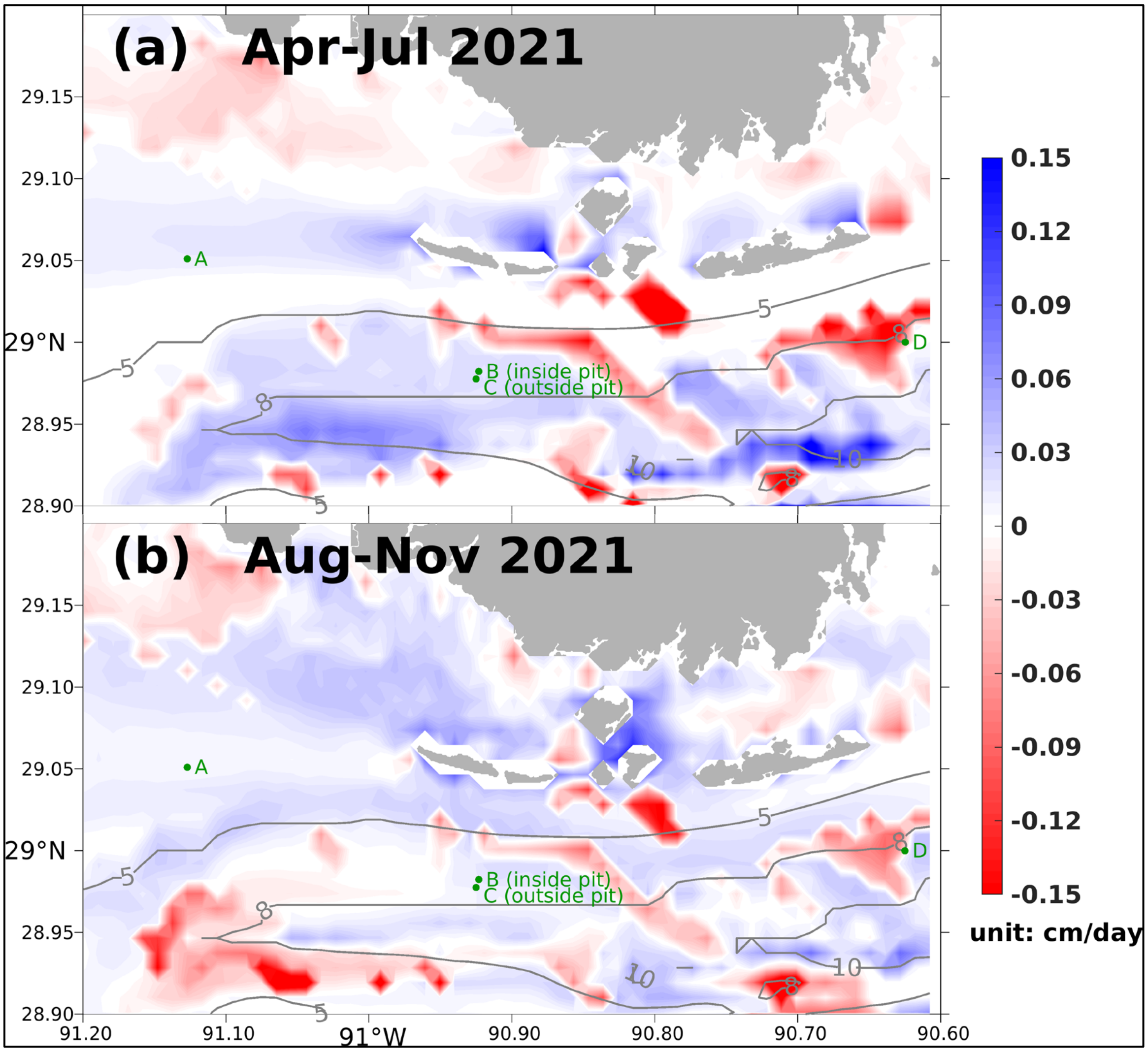

Figure 30. Spatial distribution of modeled sedimentation rates.

Top panel (a) is for April–July 2021 and the bottom panel (b) is for August–November 2021. The rates are determined by the changes in sediment thickness over a 106-day interval, comparing the modeled thickness on the sampled d. Blue represents deposition and red represents erosion.

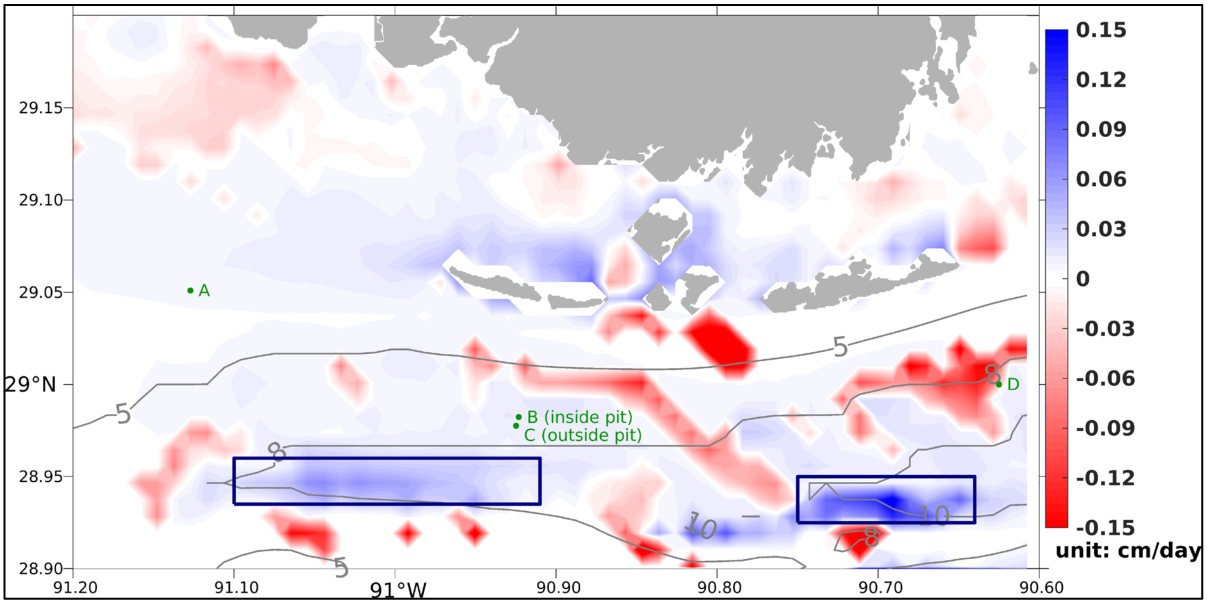

Figure 31. Spatial distribution of the long-term sedimentation rates from February to December 2021.

The sedimentation rates are derived from the temporal slopes of sediment thickness based on the model's daily output. Blue represents deposition and red represents erosion. The high-deposition regions are highlighted by dark blue rectangles.

4.7.2 Fluid Mud Probability and Bed Thickness

Fluid mud, a fine-grained, non-Newtonian slurry with a high concentration (>10 g/L), represents an intermediate stage between consolidated deposition and dilute fine sediment suspension (Zang et al. 2020). The fluid mud concentration of 10 g/L is considered a threshold that distinguishes the occurrence of fluid mud. The probability of the fluid mud occurrence (Figure 33) was calculated for the year 2021 (February to December) and found that fluid mud events are highly affected by bathymetry, the Mississippi-Atchafalaya River plumes, and the along-shore coastal currents. Two high fluid mud probability bands were detected around the river outlets (enclosed dark red curves in Figure 33), with one extending from Mississippi River point sources to 91°W within the 15 m isobath and the other one around the Atchafalaya River point sources within the 5 m isobath.

While the prevailing westward Louisiana Coastal Current significantly influences the trajectory of the Mississippi River plume and the distribution of fine-grained sediments along coastal Louisiana (Androulidakis and Kourafalou 2013; Justić et al. 2022; Schiller et al. 2011), bottom wave energy also plays a crucial role in the formation of fluid mud (Zang et al. 2020). Fluid mud thickness, also regarded as WBL thickness (section 3.3.2), is used to quantify the bottom wave energy. A thicker fluid mud layer corresponds to stronger bottom wave energy and is typically associated with a higher likelihood of fluid mud events. Annual mean fluid mud thickness indicates that the bottom wave energy is more intense within the 15 m isobath (Figure 34), particularly in areas with pronounced bathymetric gradients. As waves propagate landward, they become steeper and concentrate more energy due to shoaling effects. A higher probability of fluid mud events is expected in these shoaling regions, such as the narrow band of high fluid mud probability that extends from the Mississippi River outlets westward to 91°W. However, no apparent fluid mud event was found in the shoaling regions west of the 91°W. Instead, there is a high probability of fluid mud around the Atchafalaya River outlets within the 5 m isobath. Sediments from the Mississippi River rarely extend west of 91°W due to the long distance, whereas most sediments from the Atchafalaya River remain confined to the shallow bay, given the lower momentum discharges compared to the Mississippi River. Therefore, despite strong bottom wave energy around the 10 m isobath west of 91°W, fluid mud events are infrequent. Conversely, in Vermilion Bay and West Cote Blanche Bay, where wave energy is weaker, the substantial sediment transport by the Atchafalaya River facilitates the formation of fluid mud, particularly in the narrow channels where wave energy is concentrated.

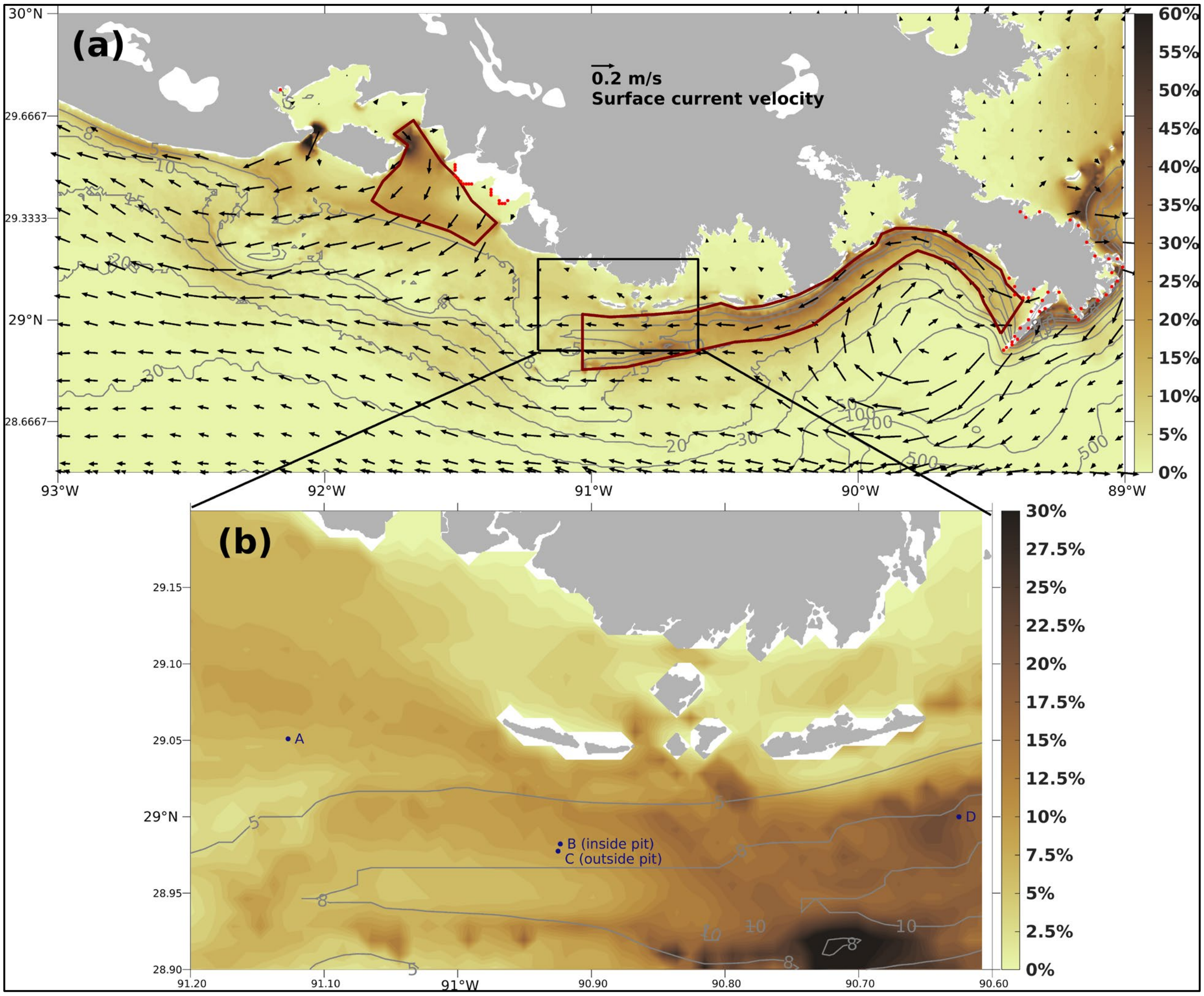

Figure 32. Spatial patterns of modeled fluid-mud probability.

Top panel (a) is for the entire computational domain and bottom panel (b) for the zoomed-in region around the sampled sites. The enclosed dark red curves in top panel (a) denote the high fluid mud probability bands around the river outlets. The arrows in top panel (a) represent surface current velocity.

The fluid mud activity is usually associated with sediment erosion. As illustrated by the annual statistics, regions with high (low) fluid mud probability (Figure 33) often overlap with net-erosion (net-deposition) areas (Figure 32). This correlation is due to the strong stirring processes due to the interaction of wind-induced waves and currents, which can also lead to seabed erosion. Furthermore, the daily time series (Figure 35) of normalized regional averages (as denoted in Figure 33b) of fluid mud concentration and bed thickness (Figure 34) shows that peaks in the former typically correspond to troughs in the latter, indicating erosion. The overall linear correlation coefficient between these parameters is significantly high, at -0.78 ($p<0.01$). Note that the bed thickness refers to the total thickness of the four predefined sediment layers at the seabed, which differs from the fluid mud thickness, defined as the thickness of the WBL, the layer between the bottom water and the upper sediment.

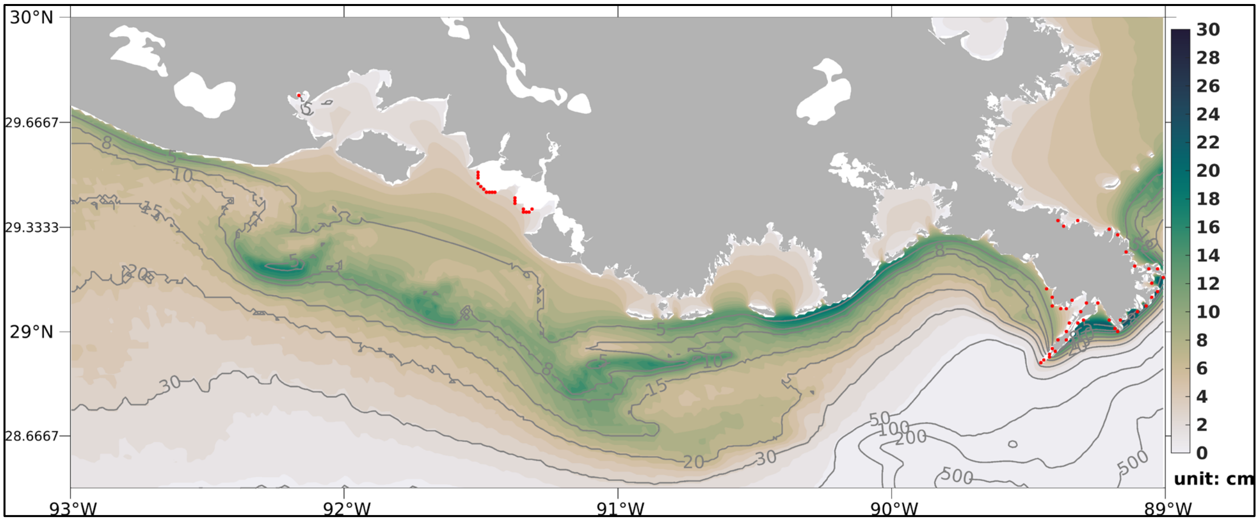

Figure 33. Spatial patterns of modeled fluid mud thickness.

The fluid mud thickness is also regarded as the thickness of WBL (see section 3.3.2) and is an indicator of the bottom wave energy. Thicker fluid mud thickness indicates stronger bottom wave energy.

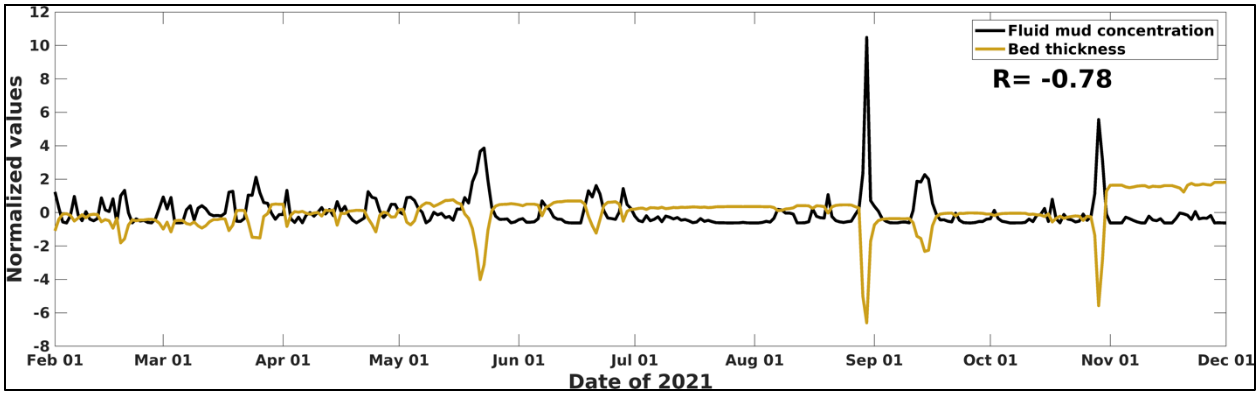

Figure 34. Daily time series of normalized regional averages of fluid mud concentration and bed thickness.

The regional averages are conducted for the region around the dredging pit, as shown in Figure 33b. The bed thickness refers to the total thickness of the four predefined sediment layers at the seabed, which differs from the fluid mud thickness, defined as the thickness of the WBL, the layer between the bottom water and the upper sediment.

5. Discussion

5.1 Occurrence of rapid sedimentation events in Louisiana shelf

Generally, the natural penetration depth of ^{7}Be ranges from the upper few millimeters or a couple of centimeters due to its short half-life (Mabit et al. 2008); however, rapid sedimentation events can lead to much deeper penetration as seen in Palinkas et al. (2005) where penetration depths of between 2-15 cm were observed. Station B, historically, has been found to have ^{7}Be penetration between 36-50+ cm during the infilling process. Thus, the presence of ^{7}Be deeper in the cores denotes sediments that were rapidly deposited sometime recently, likely due to a fluid flood event, as slower deposition would lead to lower detection rates. River discharge, wind speed, and wave height data from 2021 to 2022 located close to the sampled stations were used to determine when these fluid-mud events could have happened.

During the study, penetration depths for ^{7}Be ranging from 1 cm to 20 cm (Figure 32) were observed. Of particular interest is Station B, where, during July 2021, November 2021, and March 2022 sampling periods, ^{7}Be was detected up to 16–20 cm. No other station had more than 10 cm of ^{7}Be penetration depth across the entire study. Only Station C in March 2022 had a penetration depth of 10 cm. Thus, Station B shows the most evidence for rapid sedimentation events leading to much deeper ^{7}Be penetration. Thus, at Station B, there is evidence of at least three rapid sedimentation events, each occurring leading up to the July 2021, November 2021, and March 2022 sampling periods.

The other three stations showed much less evidence for these sedimentation events. Stations A and D (Figure 32) only had ^{7}Be penetration between 4–6cm at their deepest and 1–2cm at the shallowest. This reveals that these stations are likely not experiencing net sedimentation events, though there may be some disturbance linked to the 4–6 cm penetration depths, which were only recorded during the November 2021 and March 2022 sampling periods. This could indicate that these two stations are less impacted by fluid mud events compared to Station B. Station C was the only other location that showed evidence of rapid sedimentation events, with ^{7}Be penetration of 7 cm and 10 cm in November 2021 and March 2022. The deepest ^{7}Be penetration was observed during the months of November 2021 and March 2022 across all stations. This potentially indicates shelf-wide sedimentation events during November 2021 and March 2022, with just stronger concentration occurring at Stations B and C.

Sedimentation at B is likely connected with the Atchafalaya and Mississippi River plumes (Allison et al. 2012; Denommee et al. 2016; John T. Wells 1981; O'Connor et al. 2016; Stone et al. 2004; Upreti et al. 2019; Wright et al. 2001). O’Connor et al. (2016) determined these rivers as primary sources of sedimentation, showing that these rivers can transport sediment rapidly and over long distances. Thus, river-derived sediments are a likely source for the rapid-sedimentation events occurring before July 2021 at Station B and the November 2021 and March 2022 sampling periods. This is further supported by Station B having the highest amount of organic carbon among all stations (Figure 34), revealing potential terrestrial sources for the sediment there. Previous studies from the region indicated that wave-supported fluid mud is a key sediment transport process on the continental shelf, and multiple cycles of resuspension and deposition are likely needed for river sediment to reach the sampled stations (Zang et al. 2020; Zhang et al. 2023).

High energy events, such as hurricanes and cold fronts, bring winds and waves that can resuspend and deposit sediments across the Louisiana shelf (Twilley et al. 2016). The July 2021 fluid mud event observed at Station B can be linked to the peak in wave height and wind speed that occurred just before July 2021, indicating the passage of a storm that also led to a delayed peak in river discharge. This storm likely impacted Station B more, as there is little evidence from the other stations that sedimentation occurred there during this storm. The other possibility could be that Station B, which received a large fraction of its sediment from river sources, acted as a depocenter while other stations were subjected to net erosion.

The rapid sedimentation event observed in November 2021 likely points to Hurricane Ida and another winter storm that occurred during the beginning of November, as indicated by the wave height and wind speed spike. Hurricane Ida passed the Louisiana shelf before the third sampling period. It was a Category 4 hurricane that was active from Aug. 26 to Sept. 4, 2021. The sampled stations were located west of the eye of the hurricane. Thus, for the November 2021 sampling period, Hurricane Ida likely led to the resuspension of sediment from surrounding shoals and barrier islands and the transport of sediment offshore, leading to the observed spike in ^{7}Be sedimentation.

After Hurricane Ida, another storm occurred at the beginning of November 2021, according to the wind and wave data. This storm led to a wave height of 4 m, twice the normal height, and the wind speed was ~15 m/s, about 3-4 m/s above normal. This peak in wind speed and wave height also seems to have led to a delayed spike in water discharge at both primary rivers. Though not on the same level as Hurricane Ida, this storm, which only occurred weeks before the November 2021 sampling date (Nov. 20, 2021), could have led to another fluid-mud resuspension event further contributing to the ^{7}Be sedimentation observed during November, especially at Station B.

Stations A and D likely received their sediment primarily from the river sources and a consistent supply of resuspended fine-grained sediment from the shelf and nearby bays due to storm events (Liu et al. 2020; Rotondo and Bentley 2003; Wright et al. 2001). Evidence for this comes from the sampling in March 2022, which occurred during a time of increasing water discharge as the winter snowmelt brought the discharges to their peak in late March and early April. The 4–5 peaks in wave height and wind speed seen leading up to the March 2022 sampling period indicate the presence of successive winter storms. However, Station C, located in the furthest south, may have a different source. Zhang et al. (2023) pointed to Ship Shoal, located just south of Station C, as the likely source of sediment for this station due to its sandy nature, likely driven by events like Hurricane Ida.

5.2 Organic Matter Remineralization Post Rapid Sedimentation Events

Previous studies in this area (Zang et al. 2018; Zang et al. 2020) have shown that wave-supported fluid mud plays an important role in sediment transport. However, no study thus far has sought to understand how this sediment transport affects SOC rates. Rapid sedimentation events were identified during July 2021 at Station B, and during November 2021 and March 2022 across all stations. SOC fluxes were relatively the same within each sampling period except for July 2021, where the SOC was 2-4 times higher than other sampling periods (Figure 33). Despite this dramatic increase in SOC during the summer, all stations within the same sampling period had relatively similar SOCs in comparison to each other, including in July 2021. This is likely due to the higher seasonal temperature in summer months, which, along with higher productivity in the overlying water column in preceding months, results in faster utilization of O_2 through labile OM remineralization. The highest SOC observed across all stations occurred during July 2021, where, except for Station B, there was no evidence of a rapid sedimentation event. The events determined to occur before November 2021 and March 2022 did not lead to a different SOC when compared with the SOC measured in March 2021. Thus, rapid sedimentation events do not appear to affect SOC, but the results are complicated by the seasonal imprint of temperature and availability of labile organic matter. Thus, the quality of organic matter in resuspended sediments can be an important driver of SOC. Previous studies from the region have shown that much of the organic matter in the northern Gulf of Mexico shelf is derived from terrestrial sources (Gordon and Goñi 2004) and is likely more resilient to immediate remineralization after a resuspension event when exposed to oxic bottom water.

6. Conclusions

The study shows that fluid mud rapid sedimentation events do not lead to changes in SOC rates. This shows that these events move large amounts of sediment; however, this sediment does not seem to increase oxygen consumption. This apparent paradox suggests that the complicated overprint of temperature and the low availability of fresh labile organic matter during these events could be reasons for lower respiration rates. It is most likely that the higher temperature in this region results in rapid remineralization of labile and marine organic matter while the more resilient terrestrial organic matter is preserved in sediments. Thus, resuspension and repositioning of these sediments may not lead to a substantial increase in oxygen consumption. It is also possible that during these mobilization events, organic matter may be preferentially transported further offshore, resulting in unchanged SOC rates. Thus, this points to the capability of the shelf environment to stabilize after rapid sedimentation events. This is likely specific to the Louisiana shelf due to shallow depth and higher overall temperatures, and low organic matter content and could be different under different environmental conditions at other coastal shelf locations.

The coupled ROMS-SWAN-CSTMS+WBL model can generally capture the net deposition pattern estimated by the maximum penetration depths of ^{7}Be at the sampled sites during the periods April–July and August–November 2021, although model-measurement discrepancies are also found. These misfits are attributed to the coarse model resolution when compared to the size of the dredging pit and unrealistic modeled bathymetry. The modeled long-term sedimentation trends can help in guiding sustainable dredging operations to minimize ecological impacts on coastal regions. The model has identified two regions with high fluid mud probability: from the Mississippi River outlets to 91°W within the 10 m isobath and around the Atchafalaya River outlets within the 5 m isobath, highlighting the influence of bathymetry and coastal currents on fluid mud formation. In the former region, the high probability of fluid mud is due to both the strong wave energy and the substantial sediment delivery from the Mississippi River by the prevailing westward coastal current system. In contrast, in the latter region, despite generally weaker wave energy, the region exhibits a high fluid mud probability due to the proximity and sediment supply from the Atchafalaya River, particularly in channels where wave energy accumulates. A significantly negative correlation (-0.78; $p<0.01$) has been found between fluid mud probability and bed thickness. In regions characterized by pronounced fluid mud events, wave energy, and wave-current interactions are typically strong, actively stirring the seabed. This intense stirring process often results in seabed erosion, as indicated by a thinner sediment bed.

The benthic community can be used as an indicator of seabed conditions as dredged areas recover and as an indicator of the impact of fluid mud on the ecology of coastal environments in Louisiana. An understanding of the life history of benthic invertebrates combined with benthic community composition data allowed us to draw conclusions about the legacy and impacts of disturbance at a site that were supported by geochronology and changes in sediment grain size. For example, between spring and summer 2021, there was an event that caused a large deposit of sediment at the dredge pit at Site B, as evidenced by Be^7 penetration in the sediment. In the fall, early colonizers arrived, an indicator of recent disturbance. By the next spring, new bivalve recruits were taking advantage of the extra food and the lack of winter sedimentation. Another example occurred outside the dredge pit at Site A. There was an increase in sediment grain size in the summer of 2021, as evidenced by sediment grain size data. This was a likely sand deposition event or scouring event, but the signal was quickly erased, likely due to additional muddy deposition due to Hurricane Ida in August 2021. The field sampling effort was fortunate to catch the sand deposition or scouring event due to frequent seasonal sampling; however, benthic community composition in spring 2022 included primarily sand-dwelling species, reflecting the legacy of sediment grain size changes at that site. *Amphioxus* spp., a relatively common shelf invertebrate that is extremely easy to identify, may serve as an indicator of average annual fluid mud thickness in coastal Louisiana. This would be a key finding of this project, considering it may be difficult to track fluid mud layer thickness and frequency of occurrence over large areas of the Louisiana shelf. An indicator species would make the process of tracking fluid mud impacts much simpler and more cost-effective.

Recommendations are provided emphasizing actionable strategies to support BOEM’s sustainable management of coastal and offshore resources. First, the biochemical impacts of dredging operations are expected to be minimal, as no significant differences in benthic oxygen consumption rates were observed between areas inside and outside the dredging pit. Dredging in other shelf regions with similar environmental conditions—such as shallow depths, low organic matter content in sediments, and strong coastal current systems—is likely to result in similarly minor biochemical impacts on benthic communities.

Second, an invertebrate species, *Amphioxus* spp., is proposed as an indicator species to monitor the hard-to-track fluid mud thickness and frequency, offering a scalable and cost-effective tool for tracking ecological impacts. Last but not the least, model-generated long-term sedimentation trends should be employed to guide dredging operations, especially in high fluid mud probability areas near the Mississippi and Atchafalaya River outlets, where sedimentation is notably more pronounced than in other shelf regions. Focusing dredging efforts on these high fluid mud event areas would likely minimize environmental disruption and potentially enable re-dredging operations within a shorter timeframe, thus sustainable dredging.

Insights into benthic recovery patterns highlight the importance of considering rapid recovery transitions and the impact of sedimentation events on habitat management. Tailored, site-specific approaches are recommended for the Louisiana shelf, accounting for its unique environmental conditions, while refinements in sediment transport models and bathymetry representations will enhance predictive accuracy. Further research into offshore organic matter transport during sediment mobilization events is encouraged to deepen understanding of SOC rates and sedimentary processes. Together, these recommendations align with BOEM’s goals of balancing ecological preservation and economic priorities while managing OCS resources.

References

Abril G, Riou SA, Etcheber H, Frankignoulle M, De Wit R, Middelburg JJ. 2000. Transient, tidal time-scale, nitrogen transformations in an estuarine turbidity maximum - fluid mud system (the gironde, south-west France). Estuarine Coast Shelf Sci. 50(5):703-715.

Allison MA, Demas CR, Ebersole BA, Kleiss BA, Little CD, Meselhe EA, Powell NJ, Pratt TC, Vosburg BM. 2012. A water and sediment budget for the lower Mississippi-Atchafalaya River in flood years 2008–2010: implications for sediment discharge to the oceans and coastal restoration in Louisiana. J Hydro. 432-433:84-97.

Allison MA, Kineke GC, Gordon ES, Goi MA. 2000. Development and reworking of a seasonal flood deposit on the inner continental shelf off the Atchafalaya River. Cont Shelf Res. 20(16):2267-2294.

Androulidakis YS, Kourafalou VH. 2013. On the processes that influence the transport and fate of Mississippi waters under flooding outflow conditions. Ocean Dynamics. 63(2-3):143-164.

Ariathurai R, Arulanandan K. 1978. Erosion rates of cohesive soils. J Hydraulics Div-ASCE. 104(2):279-283.

Barras J, Beville S, Britsch D, Hartley S, Hawes S, Johnston J, Kemp P, Kinler Q, Martucci A, Porthouse J et al. 2003. Revised 2004. Historical and projected coastal Louisiana land changes: 1978-2050. Reston (VA): US Geological Survey. Open-File Report 2003-334

Bolam SG. 2011. Burial survival of benthic macrofauna following deposition of simulated dredged material. Environ Monitor Assess. 181(1-4):13-27.

Booij N, Ris RC, Holthuijsen LH. 1999. A third-generation wave model for coastal regions 1. Model description and validation. J Geophys Res C: Oceans.104(C4):7649-7666.

Borja A, Franco J, Pérez V. 2000. A marine biotic index to establish the ecological quality of soft-bottom benthos within european estuarine and coastal environments. Mar Pollut Bull. 40(12):1100-1114.

Broussard L, Boustany R. 2005. Restoration of a Louisiana barrier island: Raccoon Island case study. In: Proceedings of the 14th Biennial Coastal Zone Conference. July18–21, 2005. New Orleans, Louisiana.

Chapman DC. 1985. Numerical treatment of cross-shelf open boundaries in a barotropic coastal ocean model. J Phys Oceanogr. 15:1060-1075.

Denommee KC, Bentley SJ, Harazim D. 2018. Mechanisms of muddy clinothem progradation on the southwest Louisiana chenier plain inner shelf. Geo-Mar Lett. 38(3):273-285.

Denommee KC, Bentley SJ, Harazim D, Macquaker JHS. 2016. Hydrodynamic controls on muddy sedimentary-fabric development on the southwest Louisiana subaqueous delta. Mar Geol. 382:162-175.

Diaz RJ. 1994. Response of tidal freshwater macrobenthos to sediment disturbance. Hydrobiol. 278(1-3):201-212.

Diaz RJ, Rosenberg R. 1995. Marine benthic hypoxia: A review of its ecological effects and the behavioural responses of benthic macrofauna. Ocean Mar Biol. 33:245-303.

Draut AE, Kineke GC, Velasco DW, Allison MA, Prime RJ. 2005. Influence of the Atchafalaya River on recent evolution of the chenier-plain inner continental shelf, northern Gulf of Mexico. Cont Shelf Res. 25(1):91-112.

Fennel K, Wilkin J, Levin J, Moisan J, O'Reilly J, Haidvogel D. 2006. Nitrogen cycling in the middle Atlantic Bight: results from a three-dimensional model and implications for the north Atlantic nitrogen budget. Global Biogeochem Cycles. 20(3).

Flather R. 1976. A tidal model of the northwest European continental shelf. Memoires de la Societe Royale des Sciences de Liege. Washington (DC): Bioloigical Heritage Libarary, Smithsonian Libraries and Archives. 10:141-164.

Ghaisas NA, Maiti K, White JR. 2019. Coupled iron and phosphorus release from seasonally hypoxic Louisiana shelf sediment. Estuarine Coast Shelf Sci. 219:81-89.

Glaspie CN, Seitz RD. 2017. Role of habitat and predators in maintaining functional diversity of estuarine bivalves. Mar Ecol Prog Ser. 570:113-125.

Gordon ES, Goñi MA. 2004. Controls on the distribution and accumulation of terrigenous organic matter in sediments from the Mississippi and Atchafalaya River margin. Mar Chem. 92(1-4):331-352.

Haidvogel DB, Arango H, Budgell WP, Cornuelle BD, Curchitser E, Di Lorenzo E, Fennel K, Geyer WR, Hermann AJ, Lanerolle L et al. 2008. Ocean forecasting in terrain-following coordinates: Formulation and skill assessment of the regional ocean modeling system. J Comput Phys. 227(7):3595-3624.

Harris CK, Traykovski P, Geyer WR. 2003. Including a near-bed turbid layer in a three dimensional sediment transport model with application to the Eel River shelf, northern California. In Estuarine Coast Modeling: Proceedings of the Eight International Conference. November 3-5, 2003. Monterey, CA. American Society of Civil Engineers. p. 784-803.

Harris CK, Traykovski PA, Geyer WR. 2005. Flood dispersal and deposition by near-bed gravitational sediment flows and oceanographic transport: a numerical modeling study of the Eel River shelf, northern California. J Geophys Res C: Oceans.110(9):1-16.

Harris CK, Wiberg P. 2002. Across-shelf sediment transport: Interactions between suspended sediment and bed sediment. J Geophy Res C: Oceans. 107(C1):8-12.

Hedges JI, Stern JH. 1984. Carbon and nitrogen determinations of carbonate-containing solids. Limnol Oceanogr. 29(3):657-663.

Heiri O, Lotter AF, Lemcke G. 2001. Loss on ignition as a method for estimating organic and carbonate content in sediments: reproducibility and comparability of results. J Paleolimnol. 25(1):101-110.

Hinchey EK, Schaffner LC, Hoar CC, Vogt BW, Batte LP. 2006. Responses of estuarine benthic invertebrates to sediment burial: the importance of mobility and adaptation. Hydrobiol. 56(1):85-98.

Jaramillo S. 2008. Observations of wave-sediment interactions on a muddy shelf [dissertation]. Gainsville (FL): University of Florida. 122 p.

Jaramillo S, Sheremet A, Allison MA, Reed AH, Holland KT. 2009. Wave-mud interactions over the muddy Atchafalaya subaqueous clinoform, Louisiana, United States: Wave-supported sediment transport. J Geophys Res C: Oceans. 114(4):C04002-C04002.

Justić D, Kourafalou V, Mariotti G, He S, Weisberg R, Androulidakis Y, Barker C, Bracco A, Dzwonkowski B, Hu C et al. 2022. Transport processes in the Gulf of Mexico along the river-estuary-shelf-ocean continuum: a review of research from the Gulf of Mexico research initiative. Estuaries Coasts. 45(3):621-657.

Kineke GC, Higgins EE, Hart K, Velasco D. 2006. Fine-sediment transport associated with cold-front passages on the shallow shelf, Gulf of Mexico. Cont Shelf Res. 26(17-18):2073-2091.

Knutson TR, McBride JL, Chan J, Emanuel K, Holland G, Landsea C, Held I, Kossin JP, Srivastava AK, Sugi M. 2010. Tropical cyclones and climate change. Nat Geosci. 3(3):157-163.

Kobashi D. 2009. Bottom boundary layer physics and sediment transport along a transgressive sand body, ship shoal, south-central louisiana: Implications for fluvial sediments and winter storms [Thesis]. Baton Rouge (LA): Louisiana State University. 143 p.

Komen GJ, Hasselmann S, Hasselmann K. 1984. On the existence of a fully developed wind-sea spectrum. J Phys Oceanogr. 14:1271-1285.

Larson J, Jacob R, Ong E. 2005. The model coupling toolkit: A new fortran90 toolkit for building multiphysics parallel coupled models. Int J High Perform Comput Appl. 19(3):277-292.

Liu H, Xu K, Wilson C. 2020. Sediment infilling and geomorphological change of a mud-capped Raccoon Island dredge pit near ship shoal of louisiana shelf. Estuarine Coast Shelf Sci. 245:106979-106979.

Ma Y, Friedrichs CT, Harris CK, Wright LD. 2010. Deposition by seasonal wave- and current-supported sediment gravity flows interacting with spatially varying bathymetry: Waiapu shelf, New Zealand. Mar Geol. 275(1-4):199-211.

Mabit L, Benmansour M, Walling DE. 2008. Comparative advantages and limitations of the fallout radionuclides 137cs, 210pbex and 7be for assessing soil erosion and sedimentation. J Environ Radioactivity. 99(12):1799-1807.

Madsen OS. 1995. Spectral wave-current bottom boundary layer flows. Proc of the Coast Eng Conf. 1:384-398.

Madsen OS, Poon YK, Graber HC. 1988. Spectral wave attenuation by bottom friction: theory. Coastal Eng 1(21)34.

Madsen OS, Rosengaus MM. 1988. Spectral wave attenuation by bottom friction: experiments. Coastal Eng 1(21):849-857.

Maiti K, Carroll JL, Benitez-Nelson CR. 2010. Sedimentation and particle dynamics in the seasonal ice zone of the Barents Sea. J Mar Syst. 79(1-2):185-198.

Moriarty JM, Harris CK, Hadfield MG. 2014. A hydrodynamic and sediment transport model for the Waipaoa shelf, New Zealand: Sensitivity of fluxes to spatially-varying erodibility and model nesting. J Mar Sci Eng. 2(2):336-369.

Moriarty JM, Harris CK, Hadfield MG. 2015. Event-to-seasonal sediment dispersal on the Waipaoa River shelf, New Zealand: a numerical modeling study. Cont Shelf Res. 110:108-123.

Mullenbach BL, Nittrouer CA. 2000. Rapid deposition of fluvial sediment in the Eel Canyon, northern California. Cont Shelf Res. 20(16):2191-2212.

Munk W, Anderson E. 1948. Notes on a theory of the thermocline. J Mar Res. 7(3):276-295.

Murakami H, Delworth TL, Cooke WF, Zhao M, Xiang B, Hsu PC. 2020. Detected climatic change in global distribution of tropical cyclones. Proc National Acad Sci. 17(20):10706-10714.

Nairn R, Johnson JA, Hardin D, Michel J. 2004. A biological and physical monitoring program to evaluate long-term impacts from sand dredging operations in the United States Outer Continental Shelf. J Coast Res. 20(1):126-137.

Nairn R, Lu Q, Langendyk S (Baird and Associates, New Orleans, LA). 2005. A study to address the issue of seafloor stability and the impact on oil and gas infrastructure in the Gulf of Mexico. New Orleans (LA): U.S. Department of the Interior, Minerals Management Service. 179 p. Obligation No.: 1435-01-04-CT-335085. Report No.: OCS Study MMS 2005-043.

O'Connor MC, Bentley SJ, Xu K, Obelcz J, Li C, Miner MD. 2016. Sediment infilling of louisiana continental-shelf dredge pits: a record of sedimentary processes in the northern Gulf of Mexico. Poster presented at: 2016 Ocean Sciences Meeting. February 24, 2016. New Orleans, LA.

Obelcz J, Xu K, Bentley SJ, Li C, Miner MD, O'Connor MC, Wang J. 2016. Evolution of mud-capped dredge pits following excavation: sediment trapping and slope instability. Poster presented at: 2016 Ocean Sciences Meeting. February 24, 2016. New Orleans, LA.

Obelcz J, Xu K, Bentley SJ, O'Connor M, Miner MD. 2018. Mud-capped dredge pits: an experiment of opportunity for characterizing cohesive sediment transport and slope stability in the northern Gulf of Mexico. Estuarine Coast Shelf Sci. 208:161-169.

Orlanski I. 1976. A simple boundary condition for unbounded hyperbolic flows. J Comput Phys. 21(3):251-269.

Ou Y, Xue ZG. 2024. Hydrodynamic and biochemical impacts on the development of hypoxia in the Louisiana–Texas shelf – part 1: Roles of nutrient limitation and plankton community. Biogeosci. 21(10):2385-2424.

Palinkas CM, Nittrouer CA, Wheatcroft RA, Langone L. 2005. The use of 7be to identify event and seasonal sedimentation near the Po River delta, Adriatic Sea. Mar Geol. 222-223(1-4):95-112.

Palmer TA, Montagna PA, Nairn RB. 2008. The effects of a dredge excavation pit on benthic macrofauna in offshore Louisiana. Environ Manag. 41(4):573-583.

Penland S, Connor PF, Beall A, Fearnley S, Williams SJ. 2005. Changes in Louisiana’s shoreline: 1855–2002. J Coast Res.7-39.

Rosenberg R. 1995. Benthic marine fauna structured by hydrodynamic processes and food availability. Neth J Sea Res. 34(4):303-317.

Rossa MA, Mehta AJ. 1989. On the mechanics of lutoclines and fluid mud. J Coast Res. Special Issue No. 5. High concentration cohesive sediment transport: 51-62.

Rotondo KA, Bentley SJ. 2003. Deposition and resuspension of fluid mud on the western Louisiana inner shelf. Gulf Coast Assoc Geol Soc Trans. 53:722-731.

Safak I, Sheremet A, Allison MA, Hsu TJ. 2010. Bottom turbulence on the muddy Atchafalaya shelf, Louisiana, USA. J Geophys Res C: Oceans. 115(12).

Saha S, Moorthi S, Wu X, Wang J, Nadiga S, Tripp P, Behringer D, Hou YT, Chuang HY, Iredell M et al. 2014. The NCEP climate forecast system version 2. J Clim. 27(6):2185-2208.

Sahin C, Safak I, Sheremet A, Mehta AJ. 2012. Observations on cohesive bed reworking by waves: Atchafalaya shelf, Louisiana. J Geophys Res C: Oceans. 117(9).

Schaffner LC. 2010. Patterns and rates of recovery of macrobenthic communities in a polyhaline temperate estuary following sediment disturbance: effects of disturbance severity and potential importance of non-local processes. Estuaries Coasts. 33(6):1300-1313.

Schiller RV, Kourafalou VH, Hogan P, Walker ND. 2011. The dynamics of the Mississippi River plume: impact of topography, wind and offshore forcing on the fate of plume waters. J Geophys Res C: Oceans. 116(6).

Schimel ACG, Ierodiaconou D, Hulands L, Kennedy DM. 2015. Accounting for uncertainty in volumes of seabed change measured with repeat multibeam sonar surveys. Cont Shelf Res.111:52-68.

Shchepetkin AF, McWilliams JC. 2005. The regional oceanic modeling system (roms): A split-explicit, free-surface, topography-following-coordinate oceanic model. Ocean Modell. 9(4):347-404.

Sheremet A, Jaramillo S, Su SF, Allison MA, Holland KT. 2011. Wave-mud interaction over the muddy atchafalaya subaqueous clinoform, louisiana, united states: wave processes. J Geophys Res C: Oceans. 116(6):1-14.

Sheremet A, Mehta AJ, Liu B, Stone GW. 2005. Wave-sediment interaction on a muddy inner shelf during Hurricane Claudette. Estuarine Coast Shelf Sci. 63(1-2):225-233.

Sheremet A, Stone GW. 2003. Observations of nearshore wave dissipation over muddy sea beds. J Geophys Res C: Oceans. 108(11).

Sherwood CR, Aretxabaleta AL, Harris CK, Paul Rinehimer J, Verney R, Ferré B. 2018. Cohesive and mixed sediment in the regional ocean modeling system (roms v3.6) implemented in the coupled ocean-atmosphere-wave-sediment transport modeling system (coawst r1234). Geosci Model Dev. 11(5):1849-1871.

Skamarock WC, Klemp JB, Dudhi J, Gill DO, Barker DM, Duda MG, Huang XY, Wang W, Powers JG. 2008. A description of the advanced research wrf version 3. Boulder (CO): Nat Center Atmospheric Res. Report No.: NCAR/TN–468+STR. 74 p.

Smith JD, McLean SR. 1977. Spatially averaged flow over a wavy surface. J Geophys Res. 82(12):1735-1746.

Sommerfield CK, Nittrouer CA, Alexander CR. 1999. 7be as a tracer of flood sedimentation on the northern California continental margin. Cont Shelf Res. 19(3):335-361.

Stone GW (Louisiana State University, Baton Rouge, LA). 2000. Wave climate and bottom boundary layer dynamics with implications for offshore sand mining and barrier island replenishment in south-central Louisiana. New Orleans (LA): U.S. Department of the Interior, Minerals Management Service. 94 p. Obligation No.: 14-35-0001-30660-19911b. Report No.: OCS Study MMS 2000-053.

Stone GW, Condrey RE, Fleeger JW, Khalil SM, Kobashi D, Jose F, Evers E, Dubois S, Liu B, Arndt S. (Louisiana State University, Baton Rouge, LA). 2009. Environmental investigation of the long-term use of ship shoal sand resources for large-scale beach and coastal restoration in Louisiana. New Orleans (LA): US Dept. of the Interior, Minerals Management Service. 314 p. Obligation No.: 1435-01-04-CA-35162. Report No.: OCS Study MMS 2009-024.

Stone GW, Pepper DA, Xu J, Zhang X. 2004. Ship shoal as a prospective borrow site for barrier island restoration, coastal south-central Louisiana, USA: Numerical wave modeling and field measurements of hydrodynamics and sediment transport. J Coast Res. 20(1):70-88.

Stone GW, Xu J. (Louisiana State University, Baton Rouge, LA). 1996. Wave climate modeling and evaluation relative to sand mining on Ship Shoal, offshore Louisiana, for coastal and barrier island restoration. New Orleans, LA: U.S. Department of the Interior, Minerals Management Service. 87 p. Obligation No.: 14-35-0001-30660. Report No.: OCS Study MMS 1996-059.

Traykovski P, Trowbridge J, Kineke G. 2015. Mechanisms of surface wave energy dissipation over a high-concentration sediment suspension. J Geophys Res C: Oceans. 120(3):1638-1681.

Twilley RR, Bentley SJ, Chen Q, Edmonds DA, Hagen SC, Lam NSN, Willson CS, Xu K, Braud DW, Hampton Peele R et al. 2016. Co-evolution of wetland landscapes, flooding, and human settlement in the Mississippi River delta plain. Sustain Sci. 11(4):711-731.

Upreti K, Maiti K, Rivera-Monroy VH. 2019. Microbial mediated sedimentary phosphorus mobilization in emerging and eroding wetlands of coastal Louisiana. Sci Total Environ. 651:122-133.

Walsh KJE, McBride JL, Klotzbach PJ, Balachandran S, Camargo SJ, Holland G, Knutson TR, Kossin JP, Lee Tc, Sobel A et al. 2016. Tropical cyclones and climate change. Wiley Interdisciplinary Reviews: Climate Change. 7(1):65-89.

Wang H, Bi N, Wang Y, Saito Y, Yang Z. 2010. Tide-modulated hyperpycnal flows off the Huanghe (Yellow River) mouth, China. Earth Surf Processes Landforms. 35(11):1315-1329.

Warner JC, Armstrong B, He R, Zambon JB. 2010. Development of a coupled ocean-atmosphere-wave-sediment transport (coawst) modeling system. Ocean Modell. 35(3):230-244.

Warner JC, Sherwood CR, Signell RP, Harris CK, Arango HG. 2008. Development of a three-dimensional, regional, coupled wave, current, and sediment-transport model. Comput Geosci. 34(10):1284-1306.

Wells JT, Kemp GP. 1981. Atchafalaya mud stream and recent mud flat progradation: Louisiana chenier plain. Gulf Coast Assoc Geol Soc Trans. 31:409-416.

Williams SJ, Arsenault MA, Buczkowski BJ, Reid JA, Flocks J, Kulp MA, Penland S, Jenkins CJ. 2006. Surficial sediment character of the Louisiana offshore continental shelf region: A GIS compilation. Reston (VA): U.S. Geological Survey. Open-File Report 2006-1195. 34 p.

Williams SJ, Penland S, Sallenger AH. 1992. Atlas of shoreline changes from 1853 to 1989 : Louisiana barrier island erosion study. Reston (VA): U.S. Geological Survey. Report No: 2150. 109 p.

Williams SJ, Stone GW, Burruss AE. 1997. A perspective on the Louisiana wetland loss and coastal erosion problem. J Coast Res. 13(3):593-594.

Wilson CG, Matisoff G, Whiting PJ. 2003. Short-term erosion rates from a 7be inventory balance. Earth Surf Process Landforms. 28(9):967-977.

Wright LD, Friedrichs CT. 2006. Gravity-driven sediment transport on continental shelves: A status report. Cont Shelf Res. 26(17-18):2092-2107.

Wright LD, Friedrichs CT, Kim SC, Scully ME. 2001. Effects of ambient currents and waves on gravity-driven sediment transport on continental shelves. Mar Geol. 175(1-4):25-45.

Xu K, Bentley SJ, Li C, Chaichitehrani N, Obelcz J, O'Connor M (Louisiana State University, Baton Rouge, LA). 2019. An assessment of mudcapped dredge pit evolution on the outer continental shelf of the Gulf of Mexico. New Orleans (LA): US Dept. of the Interior, Bureau of Ocean Energy Management. 91 p. Obligation No.: GM-14-03-05. Report No.: BOEM 2022-006.

Xu K, Harris CK, Hetland RD, Kaihatu JM. 2011. Dispersal of Mississippi and Atchafalaya sediment on the Texas-Louisiana shelf: Model estimates for the year 1993. Cont Shelf Res. 31(15):1558-1575.

Xu K, Maiti K, Bargu AS, Bentley SJ, White JR, Wilson C, Xue ZG, Bales R, Barley M, Boudreaux M et al (Louisiana State University, Baton Rouge, LA). 2022. Development of a monitoring program for water quality and biogeochemical processes of Louisiana sediment borrow areas. New Orleans (LA): US Dept. of the Interior, Bureau of Ocean Energy Management. 71 p. Obligation No.: M17AC00019. Report No.: BOEM 2023-080..

Xu K, Mickey RC, Chen Q, Harris CK, Hetland RD, Hu K, Wang J. 2016a. Shelf sediment transport during Hurricanes Katrina and Rita. Comput Geosci. 90:24-39.

Xu K, Miner M, Bentley SJ, Li C, Obelcz J, O'Connor M. 2016b. Assessment of mud-capped dredge pit evolution offshore Louisiana: implications to sand excavation and coastal restoration. Abstract: 2016 Ocean Sciences Meeting. February 24, 2016. New Orleans, LA.

Xue Z, He R, Liu JP, Warner JC. 2012. Modeling transport and deposition of the Mekong River sediment. Cont Shelf Res. 37:66-78.

Zang Z, Xue ZG, Bao S, Chen Q, Walker ND, Haag AS, Ge Q, Yao Z. 2018. Numerical study of sediment dynamics during Hurricane Gustav. Ocean Modell. 126:29-42.

Zang Z, Xue ZG, Xu K, Bentley SJ, Chen Q, D'Sa EJ, Ge Q. 2019. A two decadal (1993-2012) numerical assessment of sediment dynamics in the northern Gulf of Mexico. Water (CH). 11(5):938-938.

Zang Z, Xue ZG, Xu K, Ozdemir CE, Chen Q, Bentley SJ, Sahin C. 2020. A numerical investigation of wave-supported gravity flow during cold fronts over the Atchafalaya Shelf. J Geophy Res C: Oceans. 125(9):e2019JC015269. 24 p.

Zeng X, He R, Xue Z, Wang H, Wang Y, Yao Z, Guan W, Warrillow J. 2015. River-derived sediment suspension and transport in the Bohai, Yellow, and East China Seas: a preliminary modeling study. Cont Shelf Res. 111:112-125.

Zhang W, Xu K, Herke C, Alawneh O, Jafari N, Maiti K, Clower PO, Glaspie CN, Tupitza JC, Xue ZG. 2023. Spatial and temporal variations of seabed sediment characteristics in the inner Louisiana shelf. Mar Geol. 463:107115-107115.

Zimmermann CF, Keefe CW, Bashe J. 1997. Method 440.0: Determination of carbon and nitrogen in sediments and particulates of estuarine/coastal waters using elemental analysis. Washington (DC): U.S. Environmental Protection Agency. EPA/600/R-15/009.